

1 **Shallow convective heating in weak temperature
2 gradient balance explains mesoscale vertical motions in
3 the trades**

4 **M. Janssens^{1,2}, G. George^{2,3}, H. Schulz^{4,5}, Fleur Couvreux⁶, Dominique
5 Bouniol⁶**

6 ¹Wageningen University & Research, Wageningen, The Netherlands

7 ²Delft University of Technology, Delft, The Netherlands

8 ³Max Planck Institute for Meteorology, Hamburg, Germany

9 ⁴Cooperative Institute for Climate, Ocean & Ecosystem Studies (CICOES), Seattle, WA, USA

10 ⁵University of Washington, Seattle, WA, USA

11 ⁶CNRM, Université de Toulouse, Météo-France, CNRS, Toulouse, France

12 **Key Points:**

- 13 • A realistic large-eddy simulation adequately represents vertical motion in shallow
14 mesoscale circulations recently observed in the trades
- 15 • At mesoscales, shallow convective heating causes the vertical motion, inverting the
16 classical view that circulations control shallow clouds
- 17 • Water vapour convergence with the circulations is likely key to develop the mesoscale
18 shallow convection patterns

19 **Abstract**

20 Earth's climate sensitivity depends on how shallow clouds in the trades respond
 21 to changes in the large-scale tropical circulation with warming. In all theory for this cloud-
 22 circulation coupling, it is assumed that the clouds are controlled by the field of vertical
 23 motion on horizontal scales larger than the convection's depth (~ 1 km). Yet this as-
 24 sumption has been challenged both by recent in-situ observations, and idealised large-
 25 eddy simulations (LESs). Here, we therefore bring together the recent observations, new
 26 analysis from satellite data, and a forty-day, large-domain (1600×900 km 2) LES of the
 27 North Atlantic from the 2020 EUREC 4 A field campaign, in search of new explanations
 28 for the interaction between shallow convection and vertical motions, on scales between
 29 10-1000 km (mesoscales). Across all datasets, the shallow mesoscale vertical motions are
 30 consistently represented, ubiquitous, frequently organised into circulations, and formed
 31 without imprinting themselves on the mesoscale buoyancy field. This allows us to em-
 32 ploy the weak-temperature gradient approximation, which shows that between at least
 33 12.5-400 km scales, the vertical motion balances heating fluctuations in groups of pre-
 34 precipitating shallow cumuli. That is, across the mesoscales, shallow convection controls the
 35 vertical motion in the trades, and does not simply adjust to it. In turn, the mesoscale
 36 convective heating patterns appear to consistently grow through moisture-convection feed-
 37 back. Therefore, to represent and understand the cloud-circulation coupling of trade cu-
 38 muli, the full range of scales between the synoptics and the hectometre must be included
 39 in our conceptual and numerical models.

40 **Plain Language Summary**

41 The tropical oceans are covered by shallow cumulus clouds, kept shallow by a gen-
 42 tle downward vertical motion associated with large (larger than thousand kilometres)
 43 tropical circulations. Changes in these circulations, e.g. due to warming climate, can there-
 44 fore change the shallow cloudiness, and their climatological cooling. Hence, understand-
 45 ing this cloud-circulation coupling is an important challenge. Here, we study the cloud-
 46 circulation coupling over areas of tens to hundreds of kilometres in detailed simulations,
 47 field observations and satellite data. We find that in such "mesocale" domains, it is not
 48 just the circulations that control the shallow clouds, but the heating in clusters of rainy
 49 cumuli that drives the circulations. The question is then: what controls these mesoscale
 50 cloud patterns? In the simulation we study, they develop in unusually moist layers, which
 51 are further moistened by the circulations. Since moister layers support more clouds, the
 52 clouds and circulations grow together. Our results show that on top of the classical sketch
 53 of clouds responding to large circulations, lies a dynamic mesoscale picture of two-way
 54 interactions between the two, which we must understand if we wish to predict the dis-
 55 tribution of clouds over the tropical oceans in our transient climate.

56 **1 Introduction**

57 In marine trade-wind regimes, a layer of shallow convection usually covers the at-
 58 mosphere's lower 1-3 km. In all conceptual models for such cumulus-topped boundary
 59 layers, the vertical motion on the O(1000 km) scale of a trade-wind region is an impor-
 60 tant control on the convection: Given fixed, imposed radiative cooling and horizontal cold-
 61 air advection to destabilise the column, variations in the advective heating and drying
 62 with the large-scale descent control variations in the depth and coverage of the clouds
 63 in the trades (e.g. Betts, 1973; Albrecht et al., 1979; Betts & Ridgway, 1989; Neggers
 64 et al., 2006). This view is taken, for example, in i) most Large-Eddy Simulation (LES)
 65 studies of trade-cumuli (e.g. Stevens et al., 2001; Siebesma et al., 2003; Blossey et al.,
 66 2013; Jansson et al., 2023), which prescribe a fixed large-scale descent at the 10-100 km
 67 domain scale, ii) in shallow cloud-controlling factor (CCF) analyses, which assume that
 68 co-variability between vertical motion and cloudiness depicts the clouds adjusting to the

69 vertical motion over $O(100 \text{ km})$ spatial scales (Myers & Norris, 2013; S. A. Klein et al.,
 70 2017; Scott et al., 2020), and iii) in the parameterisations that represent shallow cumuli
 71 in weather and climate models (e.g. Golaz et al., 2002; Hourdin et al., 2019; Walters et
 72 al., 2019).

73 The conceptual sketch of $O(1 \text{ km})$ scale shallow convection responding to $O(1000$
 74 $\text{km})$ scale vertical motion has served us well. Yet spatial variability in trade-wind cloudi-
 75 ness is usually much larger than 1 km (Wood & Field, 2011; Nuijens et al., 2014; Stevens
 76 et al., 2020; Denby, 2020; Janssens et al., 2021; Schulz, 2022), and vertical motion at scales
 77 much smaller than 1000 km is often many times larger than needed to balance the cli-
 78 matological radiative cooling (Schulz & Stevens, 2018; Bony & Stevens, 2019; George,
 79 Stevens, Bony, Pincus, et al., 2021; Stephan & Mariaccia, 2021). In observations taken
 80 during the 2020 EUREC⁴A field campaign (Stevens et al., 2021), this vertical motion
 81 is typically organised into $O(100 \text{ km})$ -scale Shallow Mesoscale Overturning Circulations
 82 (SMOCs, George et al., 2023), which couple tightly to the convective mass flux and cloud-
 83 base area fraction (Vogel et al., 2022). That is, in “mesoscale” domains of $O(10\text{-}1000 \text{ km})$,
 84 there is a strong coupling between shallow convection and shallow circulations, which
 85 cannot be explained by $O(1000 \text{ km})$ scale tropical circulations controlling $O(1 \text{ km})$ scale
 86 convection patterns. To explain how cloudy it is in such mesoscale domains, we must un-
 87 derstand both the processes that control the large-scale vertical motion, and those that
 88 control the mesoscale variability around it.

89 Here, we therefore examine what determines the low-level, mesoscale vertical mo-
 90 tion field. A clue is offered by idealised LESs on 100 km domains (Bretherton & Blossey,
 91 2017; Janssens et al., 2023). In these simulations, condensational heating anomalies in
 92 clusters of shallow cumulus clouds would not lead to mesoscale buoyancy storage, but
 93 instead to mesoscale ascent. That is, they satisfy a form of the “weak-temperature gra-
 94 dient” (WTG) approximation (e.g. Sobel et al., 2001; R. Klein, 2010; Raymond et al.,
 95 2015), which is commonly used to explain how heating in deep convection translates to
 96 circulations across the tropics (e.g. Held & Hoskins, 1985; Chikira, 2014; Wolding et al.,
 97 2016; Ahmed et al., 2021; Adames, 2022). In this view, mesoscale patterns in trade cu-
 98 muli are not merely a response to circulations; they directly drive them. However, be-
 99 yond these idealised LESs, we are not aware of dedicated studies that assess the validi-
 100 ty of WTG in the trade-wind boundary layer, or use it to link convection and circula-
 101 tions across the mesoscales. Therefore, this will be our primary objective.

102 We will use EUREC⁴A and satellite observations, and the realistically forced, large-
 103 domain LESs presented by Schulz and Stevens (2023) (both introduced in sec. 2), to in-
 104 vestigate the origins of shallow mesoscale ($\sim 50\text{-}400 \text{ km}$) vertical motions in the trades.
 105 Specifically, we compare the simulated and observed mesoscale fluctuations of vertical
 106 velocity, virtual potential temperature and water vapour (sec. 3). We present evidence
 107 that the mesoscale vertical motion observed in nature i) does indeed develop in mesoscale
 108 WTG balance, and ii) is remarkably well-simulated by the realistic LES. This will mo-
 109 tivate us to evaluate the LES’ mesoscale buoyancy budget, which reveals that the sim-
 110 ulated vertical motions are driven by convective heating in precipitating shallow cumuli,
 111 at all scales between $12.5\text{-}400 \text{ km}$ (sec. 4). Essentially, this suggests that across the mesoscales,
 112 we should invert the canonical picture of vertical motion controlling the shallow convec-
 113 tion.

114 To understand what controls the mesoscale vertical motion field, we must then un-
 115 derstand what determines the variability in shallow convective heating. In sec. 5, we dis-
 116 cuss whether such variability is forced upon the trade-wind boundary layer, or if the cir-
 117 culations in turn affect the convection through the moisture field, establishing a two-way
 118 coupling akin to what is found in idealised LESs. We find evidence for the latter, and
 119 end the paper by reviewing the implications for new conceptual sketches of the mesoscale
 120 trades (sec. 6).

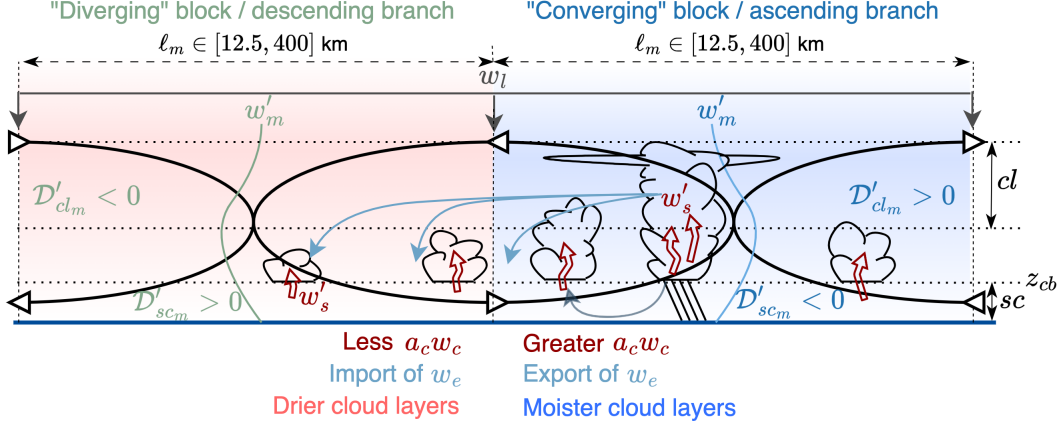


Figure 1. Conceptual illustration of a shallow circulation between mesoscale regions. A gentle large-scale descent aloft (w_l), is superimposed by mesoscale (ℓ_m) regions of subcloud-layer (sc) volume convergence $D'_{sc_m} < 0$ and divergence $D'_{sc_m} > 0$; these are the branches of coherent circulations which close in the upper cloud layer (cl), and whose vertical motion profiles are sketched as w'_m . Superimposed on these in turn are the cumulus-scale plumes and turbulence w'_s . w'_m in ascending branches is carried by greater volume fluxes $a_{cm} w_{cm}$ through deeper, precipitating cumuli with a larger cloud-base cloud cover a_c , and by export of compensating subsidence w_e towards descending branches with less strong $a_{cm} w_{cm}$. The export is achieved by waves triggered by the additional convective heating in the ascending branches, working to keep the mesoscale in weak-temperature gradient balance. Ascending branches accumulate water vapour in their cloud layers (blue vs. red), potentially driving a self-reinforcing feedback that governs the life cycle of mesoscale shallow convection.

121 2 Simulation & observation data

122 2.1 Definitions

123 To more formally distinguish mesoscale variability in a variable ψ from larger- and
 124 smaller scale fluctuations, we separate ψ into averages over regions of i) “small” scale
 125 (ψ_s , we take $\psi = \psi_s$), ii) “mesoscale” (ψ_m) and iii) “large” scale (ψ_l). Denoting spa-
 126 tial fluctuations around these averages with primes ′, they relate to each other as

$$\psi = \psi_l + \psi'_m + \psi'_s = \psi_m + \psi'_s = \psi_s. \quad (1)$$

127 For $\psi = w$ (vertical velocity), fig. 1 indicates conceptually which features fall in
 128 each scale range. We will modify the scales to which ψ_l and ψ_m refer throughout the manuscript.
 129 Yet unless stated otherwise, ψ_m will refer to 200 km, and ψ_l to 400 km-scale averages;
 130 ψ'_s then refers to sub-200 km scale fluctuations. We will also approximate certain spa-
 131 tial fluctuations ψ' with temporal fluctuations ψ'' around temporal averages $\langle \psi \rangle$, which
 132 satisfy

$$\psi = \langle \psi \rangle + \psi''. \quad (2)$$

133 All these choices are practically motivated, as explained next.

134 **2.2 ICON large-eddy simulation**

135 To interpret the shallow vertical motion observed during EUREC⁴A, we will use
 136 the 41-day (10 January to 20 February 2020) large-eddy simulations (LESs) of the cam-
 137 paign run with the Icosahedral Nonhydrostatic (ICON) model by Schulz and Stevens (2023,
 138 see their paper for further details). The simulation we study covers the North Atlantic
 139 between 60–47W and 9–16.25N at a horizontal grid spacing $\Delta x = 312$ m (ICON-312),
 140 and is forced on its vertical and lateral boundaries by reanalysis and global modeling data.
 141 A shorter simulation (1 to 7 February) over 59.75–50W and 10.5–15.5N at $\Delta x = 156$ m
 142 (ICON-156) returns similar statistics of 200-km scale cloud-base vertical motion (figs.
 143 S1–S2); we therefore choose to focus on the larger, longer ICON-312 simulation.

144 We analyse three-dimensional fields of specific humidity q_v , liquid cloud water spe-
 145 cific humidity q_c , rain-water specific humidity q_r and virtual potential temperature θ_v
 146 (all as defined by Dipankar et al. (2015), who refer to θ_v as θ_ρ), their grid-resolved ver-
 147 tical fluxes, and the velocity field $u_j = [u, v, w] = [u_h, w]$, extracted from the ICON-
 148 312 simulation at its 3-hourly output frequency, and averaged over quadratic blocks of
 149 various sizes between 5–400 km to give ψ_m .

150 In contrast to LESs departing from spatially homogeneous conditions or kilometre-
 151 scale resolution mesoscale or global models, ICON-312 simultaneously represents syn-
 152 optic variability, mesoscale processes and the large eddies of shallow convection. It also
 153 simulates longer time periods than other recent simulations of individual mesoscale weather
 154 events (Narenpitak et al., 2021; Dauhut et al., 2023; Saffin et al., 2023). Hence, the sim-
 155 ulation allows both i) comparisons against the observed statistics of mesoscale vertical
 156 motion during EUREC⁴A (Bony et al., 2017), and ii) expansions of our view on the dom-
 157 inant mesoscale balances of shallow convection to the monthly time scale. Therefore, we
 158 analyse time-averaged statistics of ψ_m , and assume they sketch the climatological mesoscale
 159 cloud-circulation coupling in trade-wind regimes.

160 **2.3 Observations**

161 We construct statistics of w , q_v and θ_v observed during EUREC⁴A from the “Joint
 162 Dropsonde Observations of the Atmosphere in Tropical North Atlantic Meso-scale En-
 163 vironments” (JOANNE, George, Stevens, Bony, Pincus, et al., 2021), which aggregates
 164 dropsondes launched along 220-km diameter circles flown by the German High Altitude
 165 and Long range (HALO) research aircraft (Konow et al., 2021). This selects the default
 166 ψ_m scale of 200 km. Since JOANNE’s circles only have a time dimension, we are forced
 167 to assume that its temporal fluctuations approximate spatial fluctuations. We follow George
 168 et al. (2023), and take ψ_m to be the average over three consecutively flown circles (roughly
 169 3 hours), and assume ψ_m'' between such “circling sets” around the campaign-mean $\langle \psi \rangle$
 170 can be reinterpreted as 200-km ψ_m' . Hence, we must assume temporal variability in larger-
 171 scale structures $\psi_l'' = 0$, which is often - but not always - tenable (sec. 3).

172 Therefore, we supplement our analysis with temporally collocated soundings from
 173 a larger-scale network of ships and a ground station (Stephan et al., 2020), as well as two
 174 products from daily overpasses of EUMETSAT’s Metop-A satellite: i) profiles of q_v es-
 175 timated by the Infrared Atmospheric Sounding Interferometer (IASI), and ii) 10 m wind
 176 speed and direction estimated by the Advanced Scatterometer (ASCAT). We use the level-
 177 2 Climate Data Record (CDR) IASI product (EUMETSAT, 2022), and the daily ASCAT-
 178 A CDR product gridded at 0.25 deg latitude and longitude (Ricciardulli & Wentz, 2016).
 179 We regrid the IASI retrievals, which are available on scan-lines perpendicular to the flight
 180 path, to the same 0.25 deg grid using nearest-neighbour interpolation. The ASCAT winds
 181 are converted to near-surface divergence \mathcal{D}_{ns} using second order finite differences. Cru-
 182 cially, \mathcal{D}_{ns} closely approximates the entire subcloud-layer average \mathcal{D}_{sc} , as we explore in
 183 detail in an upcoming companion manuscript. Hence, we can convert to cloud-base ver-
 184 tical motion w_{cb} using mass conservation in the Boussinesq limit:

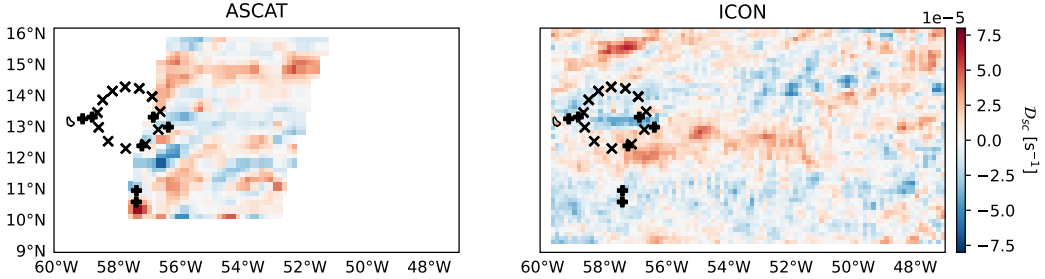


Figure 2. Fields of \mathcal{D}_{sc} as estimated from ASCAT on February 13 2020 at 14:15 UTC (left), and from the ICON simulation at 15:00 UTC (right). The ICON data are coarse-grained to the roughly 25 km native resolution of ASCAT, and further smoothed to ASCAT's roughly 50 km effective resolution for \mathcal{D}_{sc} 's. Crosses and pluses indicate dropsonde launches from HALO and radiosonde launches in the sounding network, between 12:00 and 16:00 UTC, respectively.

$$w_{cb} = \mathcal{D}_{sc} z_{cb}. \quad (3)$$

With reference to fig. 1, we loosely define the subcloud layer to range between 0 and $z_{cb} = 600$ m. Fig. 2 gives an impression of the retrieved \mathcal{D}_{sc} variability on February 13 2020 at 50 km scales, alongside its LES-derived complement.

Mirroring the LES, we average IASI and ASCAT data over square blocks. The largest scale we can attain is the average over the portion of a swath that intersects an analysis domain of 10 to 16 degrees latitude, -60 to -50 degrees longitude, in January and February 2020 (fig. 2). On average, this yields areas whose square root is roughly 400 km. This motivates our initial choice for ψ_l 's scale.

Since IASI's vertical resolution is limited below 2 km altitude (EUMETSAT, 2021), it does not capture sharp features in the boundary layer's vertical structure, such as the trade inversion (Chazette et al., 2014; Menzel et al., 2018; Stevens et al., 2018). Yet, when compared to circle circumference-averaged values from JOANNE, IASI adequately captures variability of q_v over deeper layers, such as both the subcloud and cloud-layers (fig. S3). Thus, we use the retrievals bearing their limitations in mind.

3 Mesoscale vertical motion and weak virtual temperature gradients

Fig. 2 indicates that, in line with Bony and Stevens (2019); Stephan and Mariacchia (2021); George et al. (2023), both ASCAT and ICON feature a rich variability in shallow, mesoscale divergence patterns, of many scales. To quantify the dynamic and thermodynamic variability associated with these patterns, we composite the vertical structure of w , θ_v and q_v by quartiles of \mathcal{D}_{sc} in blocks of the same scale (fig. 3). Here, we will first study w and θ_v ; we return to the co-variability with q_v in sec. 5.

At the 200 km scale, the depth and amplitude of JOANNE's w''_m , ASCAT's w'_{cb_m} and ICON's w'_m are remarkably consistent (fig. 3 a, see also figs. S2-3). Since ICON and ASCAT's spatial w'_m quartiles are robustly separated at any point in time during the campaign, we interpret this as evidence that the JOANNE-sensed w''_m is truly spatial in nature, corroborating George et al. (2023)'s findings. In reanalysis data, George et al. (2023) find this spatial structure to characterise shallow circulations, defined by columns where \mathcal{D}'_{sc_m} and its cloud-layer counterpart (\mathcal{D}'_{cl_m}) have opposing sign. The same structure is evident also in the statistics of the LES in fig. 3 a): Defining \mathcal{D}'_{cl_m} in each 200

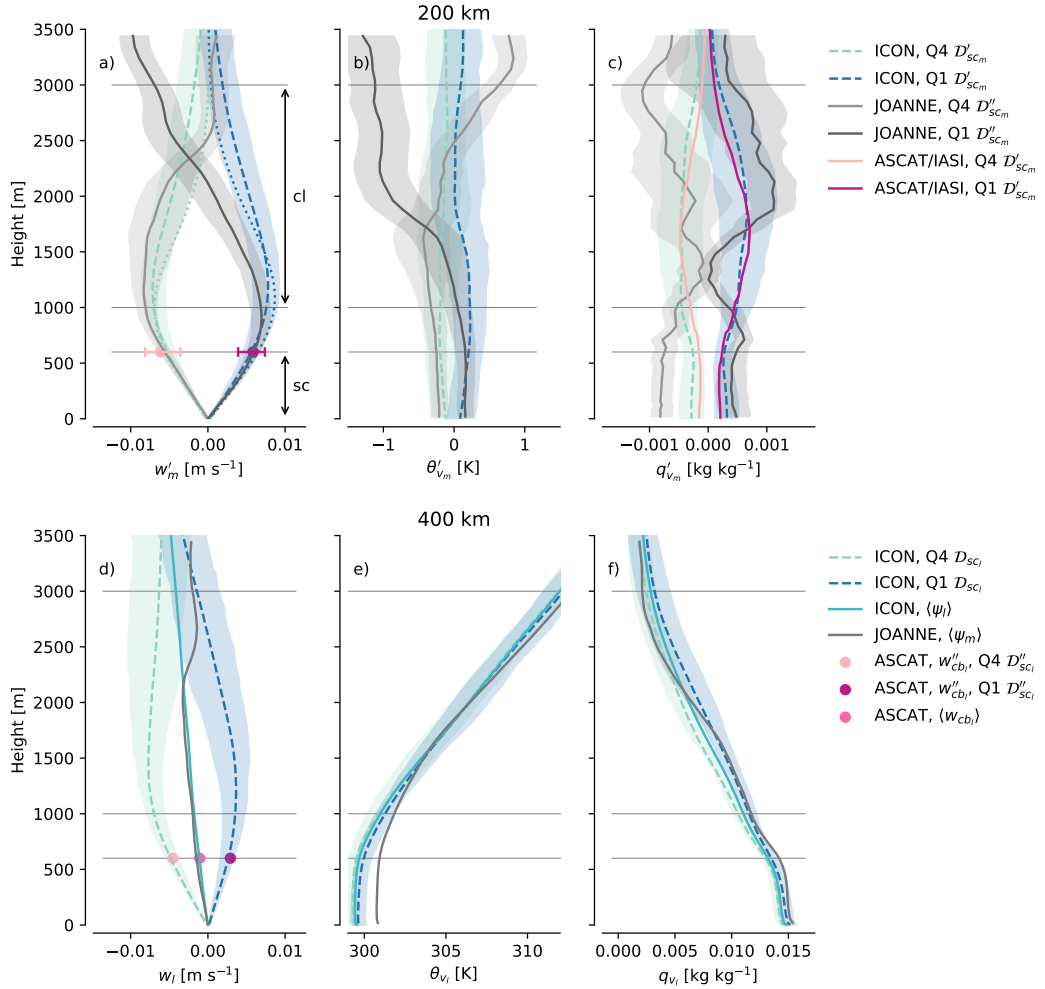


Figure 3. Spatial fluctuations of $\psi \in [w, \theta_v, q_v]$ (columns). Top row (a-c): Lowest (Q1) and highest (Q4) quartiles of 200 km-scale i) ICON ψ'_m (eq. 1) sorted by \mathcal{D}'_{sc_m} , ii) JOANNE ψ''_m (eq. 2) sorted by circling-set averaged \mathcal{D}_{sc} and iii) ASCAT w'_{cb_m} (eq. 3) and IASI q'_{v_m} , sorted by ASCAT \mathcal{D}'_{sc_m} . Bottom row (d-f): Q1 and Q4 of 400 km-scale i) ICON ψ_l sorted by \mathcal{D}_{sc_l} and ii) ASCAT w''_{cb_l} sorted by \mathcal{D}''_{sc_l} . Temporal campaign averages $\langle \psi_l \rangle$ (eq. 2) are included for all three data sets. Lines indicate time-averages of the Q1 and Q4 composites; shading indicates the interquartile range of temporal variability in ICON estimates of Q1 and Q4, and of 1000 bootstrap estimates of Q1 and Q4 in JOANNE; horizontal whiskers indicate the same for ASCAT. Dotted lines in panel a) show composites on ICON blocks which satisfy the shallow circulation criteria. The vertical extent of the layers used to define the subcloud-layer divergence \mathcal{D}_{sc} and cloud-layer divergence \mathcal{D}_{cl} are marked sc and cl , respectively.

km \times 200 block by averaging $\mathcal{D}_{\hat{\Downarrow}}'$ over a layer spanning the upper cloud layer, inversion layer and lower free troposphere, $z_{cl} \in [1000, 3000]$ m (fig. 1), we find that blocks where $\mathcal{D}'_{cl_m}/\mathcal{D}'_{sc_m} < 0$ cover $59 \pm 9\%$ of the ICON domain. This matches George et al. (2023)'s reanalysis-derived coverage fractions of $58 \pm 7\%$ very well. Additionally, 80% of the mesoscale columns with sub-cloud layer inflow and cloud-layer outflow border at least one column with a subcloud-layer outflow and cloud-layer inflow, or vice-versa. That is, ascending and descending branches of shallow circulations are spatially coherent at the mesoscale in ICON, as sketched in fig. 1. Finally, the vertical structure of w_m in mesoscale blocks where these criteria are satisfied (dotted lines in fig. 3 a) is hardly distinguishable from that of all blocks. We conclude that the w'_m fields simulated by ICON embody the statistics of the mesoscale circulations observed in nature.

Averaged over larger scales (400 km ICON blocks; ASCAT swaths), the low-level vertical motion amplitudes (w'_l) reduce in magnitude, but still vary substantially around the campaign-mean $\langle w_l \rangle$ (fig. 3 d). Since $\langle w_l \rangle$ (approximated as $\langle w_m \rangle$ in JOANNE) does balance the climatological clear-sky radiative cooling measured above the boundary layer (George et al., 2023), these results indicate that 400 km is still too small a scale for w to represent adiabatic descent with the large-scale tropical circulation; it remains eclipsed by the mesoscale signal. We will estimate a different outer scale for w'_m in sec. 4.4.

In spite of a cold and dry bias in θ_{v_l} and q_{v_l} (fig. 3 e and f, further documented by Schulz and Stevens (2023)), ICON represents w'_m , w'_l and $\langle w_l \rangle$ very well. Therefore, we will use the simulation to explore the origins of the shallow mesoscale vertical motion. To do so, we exploit that circulations develop on top of very small mesoscale buoyancy fluctuations: Compositing θ'_{v_m} on \mathcal{D}'_{sc_m} shows that θ'_{v_m} co-varies with the divergence patterns by only ~ 0.1 K across the campaign, underneath the trade inversion around 1500 m, both in ICON and in JOANNE (figs. 3 b and e). Above 1500 m, JOANNE's θ''_{v_m} grows to around 1 K. However, this variability is also present in the larger-scale sounding network (fig. S4). That is, JOANNE's larger free-tropospheric θ''_{v_m} appears to embody larger-scale, temporal variability in the lapse rate; spatial mesoscale buoyancy anomalies remain small. Also the heating rates $\partial_t \theta_v$, as far as we can estimate them, are similar between JOANNE's mesoscale circles and the larger-scale sounding network (fig. S5). In all, while the scarcity of the observational data poses limits to the strength of our conclusions, the data we do have supports the use of WTG as a useful starting point for conceptual models of shallow vertical motion in the trades.

4 Shallow circulations rooted in precipitating shallow convection

4.1 Mesoscale buoyancy budget

To formulate a WTG model, we will concentrate on the budget for θ_v , which is conserved by ICON, with two approximations. First, we treat the equation in the anelastic limit, since we consider shallow convective and internal wave phenomena over horizontal scales where sound waves may still be considered fast (e.g. R. Klein, 2010). Second, we approximate θ_v with the “liquid-water virtual potential temperature” θ_{lv} , which approximately satisfies:

$$\theta_{lv} \approx \theta_v - \left(\frac{L_v}{c_p \Pi \Theta} - \frac{R_d}{R_v} - 1 \right) \Theta(q_c + q_r) = \theta_v - a_3 \Theta(q_c + q_r). \quad (4)$$

L_v is the latent heat of vaporisation, c_p is the specific heat of dry air at constant pressure, $\Pi = (p/p_0)^{R_d/c_p}$ is the Exner function where p_0 denotes a reference pressure and R_d the gas constant of dry air, R_v is the gas constant for water vapour and Θ is a reference potential temperature scale of the boundary layer (taken to be 300 K). These variable choices identify the constant $a_3 \approx 7$, adopted from Stevens (2007)'s eq. 10. θ_{lv} has the advantage over θ_v that it is conserved over reversible condensation and evaporation,

yet when fluctuations in q_c and q_r are small or stationary, θ'_{lv} approximates the buoyancy or its tendency very well. Additionally, its vertical flux convergence closely tracks the work done by condensational heating in non-precipitating shallow cumuli (Stevens, 2007), and mesoscale fluctuations therein (Bretherton & Blossey, 2017; Janssens et al., 2023). The budget for θ'_{lv} reads:

$$\partial_t \theta'_{lv} = -\partial_x(u_h \theta'_{lv}) - \frac{1}{\rho_0} \partial_z(\rho_0 w \theta'_{lv}) - \frac{1}{\rho_0 c_p \Pi} \partial_z(\mu L_v P + R), \quad (5)$$

where ρ_0 is the reference density required to satisfy it in the anelastic limit, and ∂_t , ∂_x and ∂_z refer to differentiation in the temporal, the two horizontal and the vertical dimension, respectively. Two diabatic source terms appear: The convergence of i) radiative fluxes R , and ii) warm precipitation fluxes P , scaled by the parameter

$$\mu = 1 - \frac{0.608 c_p \Pi \Theta}{L_v} \approx 0.93, \quad (6)$$

following e.g. Bretherton and Wyant (1997). Using the definition eq. 1 and the anelastic equation of mass conservation, eq. 5 can be rewritten into a relation for θ'_{lv_m} :

$$\underbrace{\partial_t \theta'_{lv_m} + u_{h_l} \partial_x \theta'_{lv_m}}_1 = -\underbrace{u'_{h_m} \partial_x \theta'_{lv_l}}_2 - \underbrace{w_l \partial_z \theta'_{lv_m}}_3 - \underbrace{w'_m \partial_z \theta'_{lv_l}}_4 \\ - \underbrace{\partial_x [u'_{h_m} \theta'_{lv_m} - (u'_{h_m} \theta'_{lv_m})_l]}_5 - \underbrace{\partial_x [(u'_{h_s} \theta'_{lv_s})_m - (u'_{h_s} \theta'_{lv_s})_l]}_6 \\ - \underbrace{\frac{1}{\rho_0} \partial_z [\rho_0 (w'_m \theta'_{lv_m} - (w'_m \theta'_{lv_m})_l)]}_7 - \underbrace{\frac{1}{\rho_0} \partial_z [\rho_0 ((w'_s \theta'_{lv_s})_m - (w'_s \theta'_{lv_s})_l)]}_8 \\ - \frac{1}{\rho_0 c_p \Pi} \partial_z(\mu L_v P'_m + R'_m) \quad (7)$$

We estimate term 1 (storage) by taking the difference between a block's θ'_{lv_m} at time t , and the θ'_{lv_m} of the block which resides $u_{h_l} \Delta t$ upstream at time $t - \Delta t$, with $\Delta t = 3$ hr. We ignore terms 2, 3, 5, 6 and 7, as they are generally an order of magnitude smaller than the leading-order terms in the balance. This leaves terms 4 (mesoscale vertical advection) and 8 (anomalous vertical flux convergence), and the two diabatic sources.

R'_m is computed from fields of radiative heating rates, which are stored by the model once each simulated day, usually after sunset. Hence, it comprises longwave cooling only, and can be evaluated at 1/8th the frequency of the advective terms. P'_m imprints itself on the θ'_{lv_m} budget by sedimenting q_r and q_c with respect to the local flow. We compute it by reproducing ICON's rain sedimentation scheme (based on Stevens & Seifert, 2008) offline, using fields of q_r , q_c , ρ and the rain-droplet number concentration n_r , which are also stored once a day. At time steps where P and R are not available, we approximate P from offline calculations of the autoconversion and accretion rates, following Radtke et al. (2023) (see text S1), and we ignore R , for reasons that will shortly become clear. The budget terms are composited by the first and fourth quartiles (Q1, Q4) of D'_{sc_m} in 200 km blocks, and averaged over the two-month simulation period. The results are plotted in fig. 4.

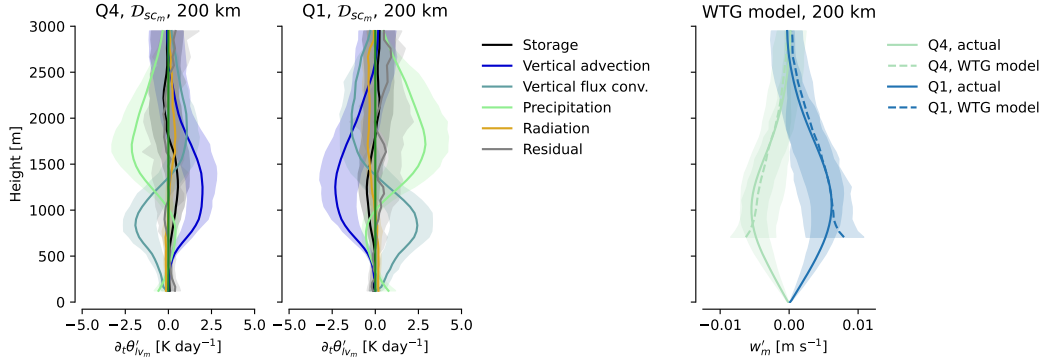


Figure 4. Left and central columns: Budgets of θ'_{lv_m} averaged over the entire ICON simulation period, in 200 km blocks, composited by D'_{scm} (Q1 and Q4), as in fig. 3. Right column: w'_m as diagnosed directly from the simulations (unbroken lines, “actual”), and from the WTG model for w'_m (eq. 8), plotted only above 700 m where gradients in θ_v become appreciable. Shading captures the temporal IQR.

In spite of a budget residual¹, a few features robustly emerge. The tendency and horizontal transport terms of θ'_{lv_m} are both smaller than 1 K day $^{-1}$ at 200 km scales, in both converging and diverging regions. This compares well to the daily-averaged heating rate differences between JOANNE and the sounding network (fig. S5). In ascending regions, we observe anomalous convergence of θ_{lv} , supported primarily by additional condensation and liquid-water transport through cumulus clouds, up to the inversion base around 1500 m. In the inversion layer and lower free troposphere, anomalous latent heating driven by precipitation takes over, while the liquid water (partly) evaporates, generating anomalous cooling. Together, these two heat sources (henceforth referred to as convective heating) balance adiabatic cooling from mesoscale ascent along the large-scale stratification. Q4 experiences largely the opposite situation; its convective heating anomalies are smaller than the large-scale average, balancing $w'_m < 0$.

Presenting a balanced budget is insufficient for a dynamical description of which term causes another to respond. However, WTG relies on a well-established principle that *does* imply causality. The cloud layer, inversion layer and free troposphere of our simulations are all stably stratified, with a Brünt-Väisälä frequency $N \approx 0.014$ s $^{-1}$. In such stably stratified layers, convective heating causes buoyancy fluctuations, which are rapidly distributed horizontally by gravity waves. This prevents θ'_v between a collection of active cumuli and their environment from growing beyond the adjustment time scale of the waves, over the horizontal area they reach (Bretherton & Smolarkiewicz, 1989; Sobel et al., 2001; Bretherton & Blossey, 2017). For our N and the first vertical half-wavelength of our heating anomaly ($h_w \approx 2500$ m), these waves propagate horizontally at roughly $c \approx Nh_w/\pi \approx 12$ m s $^{-1}$; that is, the first wave mode spreading uniformly in all directions would relax θ'_{v_m} to zero over a 200 km region over a time scale of less than 3 h. Instead of raising θ'_v , the θ'_v sources cause a collective vertical motion over such areas, as discussed further in sec. 4.3; the adiabatic cooling with this motion balances the budget.

¹ This may derive from a combination of the following: i) the small budget contributions we have ignored, ii) numerical errors in our central difference approximations of a) tendencies over the 3 hour time intervals that the ICON data is stored at and b) horizontal gradients over 200 km m-blocks, iii) errors in our computation of P'_m , and iv) the missing sub-grid contributions to $(w'_s \theta'_{lv_s})$.

316 In all, we may simplify eq. 7 to a reasonable model of w'_m (right column, fig. 4):

$$w'_m \approx - \left(\frac{1}{\rho_0} \partial_z \left(\rho_0 F_{\theta'_{lv_m}} \right) + \frac{1}{\rho_0 c_p \Pi} \partial_z (\mu L_v P'_m) \right) / \partial_z \theta_{lv_l} \quad (8)$$

317 where

$$F_{\theta'_{lv_m}} = (w'_s \theta'_{lv_s})_m - (w'_s \theta'_{lv_s})_l. \quad (9)$$

318 This model holds well above the height where θ_{lv_l} becomes stably stratified, around
 319 700 m (right column of fig. 4). Below this height, eq. 8 diverges as $\partial_z \theta_{lv_l} \rightarrow 0$, reflecting
 320 the WTG approximation's inability to predict w'_m beyond the vertical level where
 321 the heat source acts (Romps, 2012a). Instead, one commonly assumes that w'_m returns
 322 linearly to zero at the surface (Sobel & Bretherton, 2000; Raymond & Zeng, 2005; Daleu
 323 et al., 2015), which fig. 3 supports. We could alleviate this ad-hoc approximation some-
 324 what by analysing the equations in a damped-gravity wave framework (e.g. Kuang, 2008;
 325 Romps, 2012b). We still present our results in the WTG approximation, because it shows
 326 most directly that the buoyancy source anomaly driving the circulations is situated in
 327 the cloud layer (fig. 4); the sub-cloud layer must adjust to the subsequent vertical pres-
 328 sure gradient by also ascending or descending adiabatically (Romps, 2012b). Thus, at
 329 200 km scales, and over a whole month of trade-wind weather (denoted by the shading
 330 in fig. 4), the vertical profile of w'_m balances the production of mesoscale buoyancy fluc-
 331 tuations by heating in mesoscale patterns of shallow, precipitating convection.

332 4.2 Lacking mesoscale radiative cooling anomalies

333 Our results de-emphasise the importance of direct, mesoscale radiative cooling anom-
 334 alies in destabilising shallow circulations: Their contributions to the anomalous heating
 335 is negligible (golden lines in fig. 4). These results run counter to the idea that the anom-
 336 alous q'_{v_m} associated with the circulations (fig. 3 c and f) would result in a horizontal ra-
 337 diative cooling differential, which could feed back on and strengthen the circulations. Such
 338 an effect is thought to be key for the self-aggregation of deep convection in cloud-resolving
 339 models (e.g. Muller et al., 2022, and references therein), and has been suggested to be
 340 sufficiently potent to drive shallow circulations in the subtropics too (Naumann et al.,
 341 2017; Stevens et al., 2018; Schulz & Stevens, 2018; Naumann et al., 2019; Prange et al.,
 342 2023). Yet, our results are in line with the simulations by Bretherton and Blossey (2017)
 343 and EUREC⁴A observations (George et al., 2023), which indicate no relationship between
 344 clear-sky radiative profiles derived from the set of dropsondes released during EUREC⁴A
 345 (Albright et al., 2021) and 200 km-scale vertical motion.

346 The small radiative *cooling* observed in converging regions (fig. 4 central panels)
 347 might help destabilise them to convection, and thus feed back on the circulations through
 348 additional convective heating. This may especially be true for large cloud anvils, which
 349 ICON largely misses (Schulz & Stevens, 2023), and for 3D radiative cooling off cloud sides
 350 (Klinger et al., 2017), which are not simulated. Furthermore, the ICON simulations lack
 351 the elevated moist layers sensed by JOANNE (fig. 3 c), which may play an important
 352 role in creating larger radiative cooling contrasts (Prange et al., 2023; Fildier et al., 2023).
 353 Hence, there are still lessons to learn about the role of radiation in the mesoscale cloud-
 354 circulation coupling.

355 4.3 Mass fluxes, compensating subsidence and variability in active cloudi- 356 ness

357 Where in a mesoscale block does shallow, mesoscale ascent or descent take place,
 358 and how does it relate to shallow cloudiness? To answer this, we decompose w_m into the

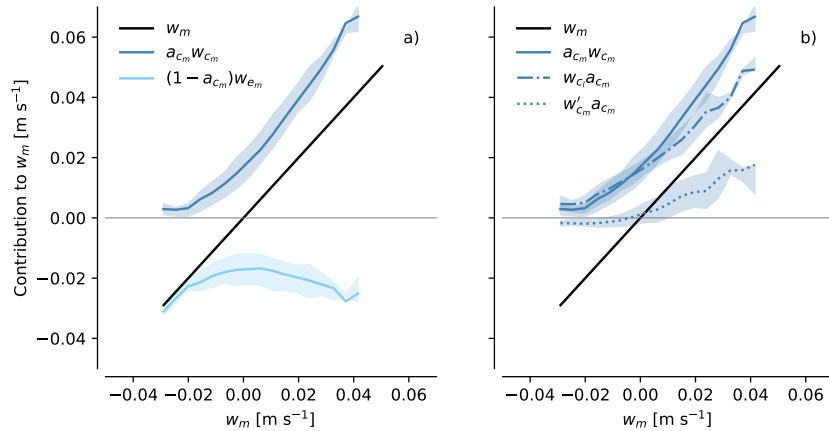


Figure 5. 200 km-scale w_m at a height of 970 m diagnosed in ICON, broken down at each w_m according to eq. 10 (a), and eq. 11 (b). Shading indicates the temporal interquartile range.

vertical motion w_{cm} averaged over a mesoscale block's cloudy area fraction a_{cm} , and the vertical motion in the environment w_{em} . $a_{cm}w_{cm}$ is the cloud-conditioned volume flux, which in the anelastic limit varies horizontally in proportion with the mass flux. At 970 m altitude, where w_m reaches its maximum (fig. 3), mass conservation for a 200 km block then demands

$$w_m = a_{cm}w_{cm} + (1 - a_{cm})w_{em}, \quad (10)$$

Fig. 5 a) displays both contributions to w_m , binned by w_m itself. It shows that spatial variability in w_m is due primarily to variability in the ascent within cumulus clouds ($a_{cm}w_{cm}$, dark blue line), because this ascent does not need to balance the compensating subsidence in cloud-free regions ($(1 - a_{cm})w_{em}$, dark blue line) within a mesoscale block. The WTG framing suggests why: The spectrum of gravity waves triggered by the heating in cumuli with upward mass fluxes rapidly carry the mass fluxes' compensating subsidence beyond a 200 km block boundary (Bretherton & Smolarkiewicz, 1989; Nicholls et al., 1991; Mapes, 1993). When $a_{cm}w_{cm}$ varies between mesoscale blocks, blocks with smaller $a_{cm}w_{cm}$ have less convective heating (Q4 vs Q1 panels in fig. 4), and trigger waves of smaller depth and amplitude than blocks with larger $a_{cm}w_{cm}$. Hence, they are unable to export the same amount of compensating subsidence as they receive, and become reservoirs of environmental descent, as we observe at $w_m < 0$, where $a_{cm}w_{cm}$ almost returns to zero, and $w_m \approx (1 - a_{cm})w_{em}$.

Our results dovetail with other EUREC⁴A observations (Vogel et al., 2022), which show that mesoscale variations in $a_c w_c$ co-vary strongly with w_m at cloud base. In fact, the subcloud-layer mass budget which Vogel et al. (2022) solve to diagnose balances between $a_{cm}w_{cm}$, $(1 - a_{cm})w_{em}$ (interpreted as an entrainment velocity) and w_m (their eq. 1), is conceptually indistinguishable from our eq. 8 evaluated at cloud base and partitioned according to eq. 10 (Stevens, 2006; Vilà-Guerau De Arellano et al., 2015), if $\partial_z P'_m$ is small. This latter assumption appears to hold well at cloud base in both observations (Albright et al., 2022) and the LES (fig. 4).

George, Stevens, Bony, Klingebiel, and Vogel (2021); Vogel et al. (2022) relate variability in $a_{cm}w_{cm}$ to variability in the cloud fraction itself, essentially assuming

$$a_{c_m} w_{c_m} = a_c w_{c_l} + a_c w'_{c_m} \approx a_c w_{c_l}, \quad (11)$$

i.e. that stronger mass fluxes express themselves in terms of larger a_c at a rather constant mean ascent through the clouds w_{c_l} , and not through variability in w_{c_m} between mesoscale blocks, w'_{c_m} . In fig. 5 b), we decompose $a_{c_m} w_{c_m}$ according to eq. 11 in the ICON simulation. It agrees with earlier observations that increases in $a_{c_m} w_{c_m}$ are primarily related to variability in a_{c_m} (Lamer et al., 2015; Sakradzija & Klingebiel, 2020; Klingebiel et al., 2021), though variability in w_{c_m} cannot be neglected in areas of strong mesoscale ascent. The classical picture of trade-wind cloud-circulation coupling would then suggest that w_m controls the cloud fraction in the trades. It is likely that w_m affects the cloudiness (sec. 5), but WTG physics emphasise that it cannot be the only direction in the relationship: In the cloud layer, w'_m results primarily from the mesoscale variability in the fraction of active cumulus clouds.

398 4.4 Cloud-layer vertical motion variability across the mesoscales

399 Does convective heating variability drive circulations also at other scales than the
400 200 km scale analysed thus far? To answer this question, we expand our simulation-observation
401 comparison and WTG analysis to the full spatial scale ranges represented by ICON and
402 ASCAT. Specifically, we compute w_m and its WTG approximation over block sizes $\ell_m \in$
403 $[5-800]$ km in ICON, and $\ell_m \in [25-400]$ km in ASCAT, and take the standard deviation
404 σ_w at each scale, at a height of 1000 m. Fig. 6 shows that in ICON, these vertical
405 motion amplitudes reduce as $\sigma_w(\ell_m) \sim \ell_m^{-1}$ for $\ell_m \in [5-40]$ km, as $\sigma_w(\ell_m) \sim \ell_m^{-\frac{1}{2}}$
406 for $\ell_m \in [40-300]$ km, and again as ℓ_m^{-1} at the largest scales. The results are in close
407 agreement with ASCAT estimates (square pink blocks), with the ℓ^{-1} scaling of divergence
408 amplitudes in the EUREC⁴A sounding network found by Stephan and Mariaccia
409 (2021), with the vertical motion contained only in blocks satisfying the SMOC criteria
410 (dotted lines), and with the predictions from the WTG model eq. 8 for $\ell \in [12.5-400]$
411 km (crosses). That is, we may consider the cloud-layer vertical motion in the trades to
412 be the ever-weakening imprint of shallow convective thermal forcing across the mesoscales.

413 Only at 700 km does σ_w cross the magnitude of $\langle w_l \rangle$ (horizontal line in fig. 6). This
414 intersection scale ℓ_i is affected by the dropoff in σ_w at the largest scales of the limited-
415 area simulation, which may be a truncation effect. Hence, ℓ_i could be even larger. Yet,
416 $\ell_i \approx 700$ km closely matches the decorrelation length in w calculated from a previous
417 ICON simulation by Bony and Stevens (2019). We therefore suggest that one may in-
418 terpret 700 km as a conservative estimate for the upper boundary to the non-divergent,
419 mesoscale flow. Below this scale, divergence in the shallow cloud layer is dominated by
420 the signal of mesoscale circulations, and only robustly above it does one recover the sig-
421 nal expected from the large-scale tropical circulation.

422 5 What controls mesoscale patterns of shallow convective heating?

423 While we have emphasised that shallow convective heating is necessary to produce
424 shallow mesoscale vertical motions in the trades, a complete picture of the cloud-circulation
425 coupling still requires an explanation for what sets the mesoscale patterns of shallow con-
426 vention. On one hand, they may embody rapid adjustment to mesoscale variations in
427 external forcings on the trade-wind boundary layer. In this limit, w'_m is the consequence
428 of these forcings, best understood through rather strict quasi-equilibrium interpretations
429 (Emanuel et al., 1994). However, shallow mesoscale convective heating patterns also de-
430 velop spontaneously under a range of spatially homogeneous forcings in LES (Jansson
431 et al., 2023). In this limit, mesoscale patterning results from self-reinforcing feedbacks
432 between the shallow convection and the shallow circulations, best understood through
433 theories of convective self-organisation.

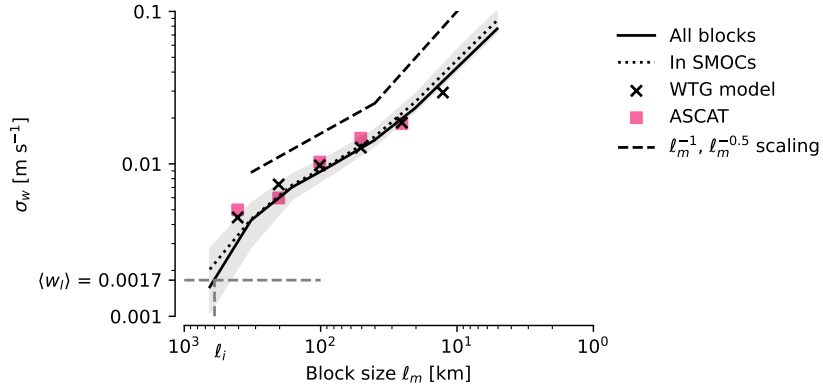


Figure 6. Variability in w_m as a function of block size ℓ_m at a height of 970 m ($\sigma_w(\ell)$), computed in ICON over all blocks (unbroken line), blocks belonging to SMOCs (dotted line) and estimated using the WTG balance eq. 8 (crosses). σ_w estimated from ASCAT is indicated in pink squares. The campaign-mean vertical motion $\langle w_l \rangle$ and its intersection scale ℓ_i are indicated by broken grey lines, while the other broken lines illustrate scaling as ℓ_m^{-1} and $\ell_m^{-\frac{1}{2}}$. Shading indicates the temporal interquartile range of σ_w at each scale.

While we leave it to future studies to elucidate where between these limits the trades lie, we present a few process-level observations from the LES to guide such efforts. To do so, we trace the time-evolution of 200 km blocks along Lagrangian trajectories with the 200 km-scale horizontal velocity at a height of 1500 m. We extract trajectories from ICON through successive 3-hourly first-order backwards finite differences (into the past) and forwards differences (into the future), launched from all 200 km blocks in the domain, at local noon and midnight. This gives us 448 trajectories at 79 launch times. We stop tracing each trajectory at a lead and lag time of 9 hours, or when the domain boundary is encountered, and assume these trajectories track coherent air masses, following e.g. Eastman et al. (2021); Lewis et al. (2023); Saffin et al. (2023). At each launch time, we extract the quartile of trajectories with the largest $-\mathcal{D}_{sc_m}$ (Q1 \mathcal{D}'_{sc_m}), and the mean trajectory. Fig. 7 a shows the evolution of both Q1 w_m (unbroken lines) and the mean w_m (dotted lines), averaged over all launch times.

With respect to the mean w_m , Q1 blocks possess anomalous cloud-layer ascent already at 9 hour lead times. Over the following 18 hours, w_m robustly amplifies and decays around its zero-lag peak (grey line, corresponding to ICON Q1 in figs. 3 a and fig. 4). Throughout the strengthening phase of its life cycle, w_m remains balanced by convective heating following eq. 8; the heat flux convergence and latent heating achieving this balance are plotted in fig. 7 b.

Is the increasing convective heating controlled by mesoscale forcing? Were it governed by anomalously strengthening surface buoyancy fluxes $(w'\theta'_{lv})_{m,0}$ along a Q1 trajectory, one would expect the convergence of $(w'\theta'_{lv})_m$ throughout the subcloud- and cloud-layers to adjust to any changes in $(w'\theta'_{lv})_{m,0}$ within an eddy-turnover time (Stevens, 2007; Bretherton & Park, 2008; Bellon & Stevens, 2013). We estimate this surface-controlled heating rate as the flux convergence through the subcloud layer

$$Q_s = -\frac{(w'\theta'_{lv})_{m,z_{cb}} - (w'\theta'_{lv})_{m,0}}{z_{cb}}. \quad (12)$$

The evolution of Q_s along Q1 trajectories is included as vertical lines in fig. 7 b.

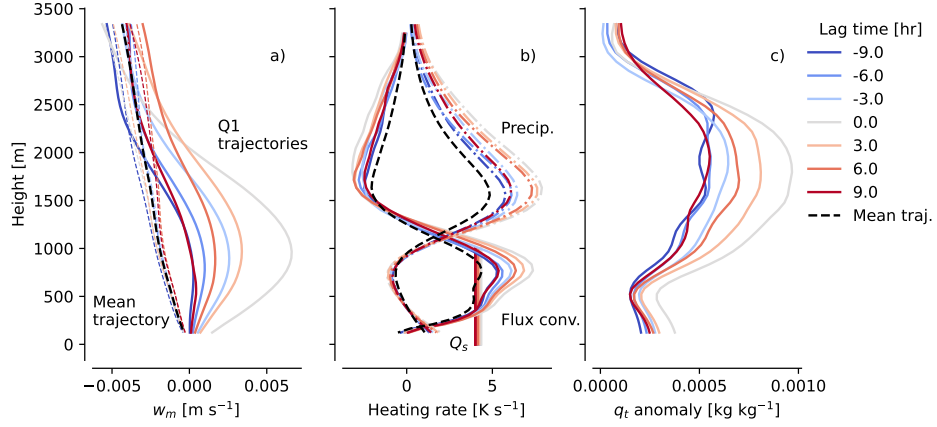


Figure 7. Profiles along Lagrangian trajectories characterising the evolution in the quartile of 200 km blocks with the strongest $D_{sc,m}$ at zero lag, traced from 9 hour lead to 9 hour lag times along Lagrangian trajectories through the ICON LES. a) Vertical motion, where unbroken lines indicate trajectories along Q1 blocks, dotted lines indicate the evolution along the mean over all blocks, and black, broken lines represent the time-average over an average trajectory; b) θ_{lv_m} heating rates from eq. 8, decomposed into contributions from the convergence of $(w'\theta'_{lv})_m$ (unbroken lines) and P_m (dash-dotted lines), and the evolution of the surface-controlled heating Q_s (vertical lines, eq. 12); c) q_t anomaly in Q1 trajectories with respect to a mean trajectory. All profiles are averaged over the 79 launch times.

As expected, Q_s explains the resolved flux convergence throughout the sub-cloud and cloud layers averaged over a *mean* trajectory (black dashed lines). However, in Q1 blocks, the cloud-layer convergence of $(w'\theta'_{lv})_m$ far exceeds the quasi-stationary Q_s ; so does the precipitation-driven latent heating. Hence, the growth of the cloud-layer heating and w_m cannot be explained by rapid adjustment to $(w'\theta'_{lv})_{m,0}$ alone, as would be expected if w_m were driven by sea-surface temperature (SST) anomalies (Park et al., 2006; Acquistapace et al., 2022; Chen et al., 2023). There is also no robust signal of strengthening anomalous vertical motion aloft in the hours prior to the convection peak, as one would expect if the convection in Q1 blocks were consistently triggered by variability in free-tropospheric w_m (Narenpitak et al., 2021) or slow downwards-propagating gravity waves (Stephan & Mariaccia, 2021). Hence, we find no evidence in the LES that mesoscale SST anomalies and descending vertical velocity modes are primary sources of mesoscale heterogeneity in shallow convection and cloudiness.

So does w_m instead grow through a self-reinforcing feedback? Fig. 7 c shows that Q1 trajectories possess anomalously moist cloud layers compared to an average trajectory already 9 hours before the convection peaks, and that q'_{t_m} grows further towards the peak. To attribute the source of this accumulation, we pose a budget for q_{t_m} along a trajectory, along the lines of eq. 5:

$$\underbrace{\partial_t q_{t_m}}_{\text{Tendency}} = \underbrace{-w_m \partial_z q_{t_m}}_{\text{Vertical advection}} - \underbrace{\frac{1}{\rho_0} \partial_z (\rho_0 w'_s q'_{t_s})_m}_{\text{Vertical flux conv.}} + \underbrace{\frac{1}{\rho_0} \partial_z P_m}_{\text{Precipitation}} + \underbrace{\mathcal{R}}_{\text{Residual (hor. trans.)}}, \quad (13)$$

where we associate the residual \mathcal{R} with the horizontal transport out of a mesoscale column as it is translated along a trajectory. We evaluate terms in this budget over both

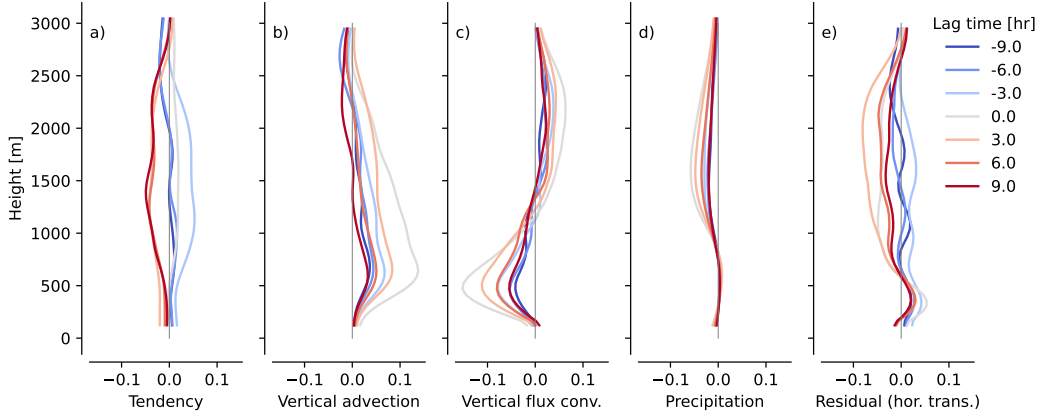


Figure 8. Terms in the moisture budget eq. 13, averaged over the trajectories in Q1 blocks, relative to the same terms, averaged over a mean trajectory. The terms are then averaged over all launch times. The units are $\text{g kg}^{-1} \text{ hr}^{-1}$.

Q1 trajectories and mean trajectories, and plot the difference in fig. 8. It shows that q'_{t_m} in Q1 grows through the vertical advection with w'_m into the lower cloud layer (fig. 8 b), is transported to the upper cloud layer by anomalously strong small-scale fluxes (fig. 8 c), and is opposed by precipitation and horizontal export (fig. 8 d, e). Because the sinks do not balance the sources while the vertical motions strengthen, $\partial_t q_{t_m} > 0$. That is, mesoscale circulations aggregate q_{t_m} and moist-static energy into more strongly convecting regions; they have a negative gross moist stability (Raymond et al., 2009). These findings are in line with the evolution predicted in case studies with idealised LESs (Bretherton & Blossey, 2017; Narenpitak et al., 2021; Janssens et al., 2023) and a numerical weather prediction model (Saffin et al., 2023). In fact, all terms in fig. 8 qualitatively match those from the earlier studies. At zero lag, this gives rise to rather deep (3-4 km) layers of $q'_{t_m} \approx q'_{v_m} \sim 1 \text{ g kg}^{-1}$, which closely match the IASI retrievals (fig. 3 c). If, as the LES studies propose, q'_{t_m} encourages subsequent convection, then w_m is controlled both by the processes that determine the vertical distribution of q_{t_m} more than 9 hours in advance of a convective peak (e.g. Aemisegger et al., 2021; Villiger et al., 2022), and a moisture-convection feedback.

However, it remains unclear exactly how the cloud-layer moisture anomalies would stimulate the convection: They could prevent entrainment drying (Janssens et al., 2023), or encourage precipitation (Nuijens et al., 2009; Radtke et al., 2023), which again drives latent heating (fig. 4), and could drive subsequent mass fluxes on cold pool edges (Dauhut, personal comm.). Yet a subcloud layer plume must reach high into the cloud layer before it can fully capitalise on the moisture lobe, whose peak is around 1500 m. At this height, peak anomalous heating has already been achieved (around 1000 m). Hence, there must be other processes that explain the anomalous mass fluxes already observed near cloud base (fig. 5). The most likely of these appears to be associated with the subcloud layer w_m , whose vertical moisture advection is appreciable at cloud base (fig. 8 b) owing to the large, negative $\partial_z q_{t_m}$ across the trade-wind transition layer (Augstein et al., 1974; Yin & Albrecht, 2000; Albright et al., 2023). This moistening approximately balances the anomalous flux divergence of q_t out of the subcloud layer (fig. 8 c). If these fluxes are in quasi-equilibrium with the boundary layer moistening courtesy of the circulations (e.g. Raymond, 1995; Emanuel, 2019), or are viewed as a triggered process that lags the heating-induced mass convergence (Yang, 2021), a conceptual model might be completed.

513 However, even if we succeeded in explaining how simulated moisture anomalies lead
 514 to simulated vertical motion, questions remain regarding the realism of the simulation.
 515 Specifically, while ICON and IASI agree that the ascent in Q1 blocks primarily corre-
 516 lates to cloud-layer q'_{v_m} , ascending circles of EUREC⁴A dropsondes correspond primar-
 517 ily to *subcloud* layer q'_{v_m} (fig. 3 c; George et al., 2023). All three data sets have weak-
 518 nesses that may explain these differences. The simulation may inadequately resolve sharp
 519 regime changes in convection at cloud base (Stevens et al., 2001) and over the inversion
 520 (Schulz & Stevens, 2023), “diffusing” the water vapour too smoothly in the vertical. IASI’s
 521 vertical resolution is too coarse to sense the sharp structures found in surface lidar (Chazette
 522 et al., 2014) or dropsonde data (fig. S3; Stevens et al., 2018). Finally, JOANNE does not
 523 sample spatial water vapour structure within the circles enclosed by its dropsondes, and
 524 contains more than an order of magnitude fewer data points than the other sources. At
 525 least part of the difference appears to stem from JOANNE’s low temporal sampling (grey
 526 shading in fig. 3 a-c). Yet if JOANNE is right, the simulated evolution of w'_m is called
 527 into question, because JOANNE suggests that the convective inhibition atop the trade-
 528 wind subcloud layer is larger than in the LES, allowing moist, buoyant subcloud layers
 529 to develop and persist. Such inhibition would disconnect the convective heating from its
 530 subcloud layer source, and could dampen the resultant circulation if it cannot accumu-
 531 late subcloud-layer water vapour quickly enough to overcome the inhibition. Hence, we
 532 also require more careful observations of the relation between lower-tropospheric water
 533 vapour and low-level vertical motions, e.g. by conditioning the moisture observed by sur-
 534 face lidars on scatterometer winds.

535 Finally, we require explanations for the decaying portion of the life cycle in Q1 blocks,
 536 where q'_{t_m} remains large, but w_m , convective heating and moisture convergence subside
 537 (fig. 7, fig. 8 b). Is the generation of cold pools at peak precipitation responsible? Their
 538 subcloud layer divergence under a cloud cluster opposes the subcloud-layer convergence
 539 otherwise observed (e.g. fig. 12 of Savazzi et al., 2024), perhaps disabling subcloud layer
 540 thermals from reaching cloud base and sustaining the convective heating pattern (Narenpitak
 541 et al., 2023). Such a mechanism, which relies on unconstrained warm rain microphysics
 542 schemes (Van Zanten et al., 2011), deserves further study.

543 6 Summary and outlook

544 We have ventured to reassess our first-order conceptual understanding of the cou-
 545 pling between shallow convection in trade-wind regimes, and vertical motions on hor-
 546 izontal scales much larger than the depth of the convection. Traditionally, the trades are
 547 viewed as areas where the large-scale tropical circulation descends, and this subsidence
 548 (w_l) controls shallow convection. However, in satellite retrievals, in-situ observations and
 549 realistic large-eddy simulations from the EUREC⁴A field campaign, we consistently find
 550 shallow vertical motion amplitudes over 200 km domains which are many times larger
 551 than what the traditional theory demands (fig. 3), matching other recent studies (Bony
 552 & Stevens, 2019; Stephan & Mariaccia, 2021; George et al., 2023). These shallow mesoscale
 553 vertical motions (w_m) blanket the lower atmosphere, are often organised in shallow cir-
 554 culations and develop without creating large, mesoscale buoyancy anomalies. That is,
 555 the simulated cloud-layer buoyancy budget satisfies a Weak Temperature Gradient (WTG)
 556 balance (fig. 4) between scales of at least 12.5–400 km (fig. 6) across a month of realis-
 557 tic weather.

558 To explain the origins of w_m , we evaluate the buoyancy budget, which shows that
 559 w'_m balances mesoscale fluctuations in convective heating, partitioned between heat flux
 560 convergence and rain sedimentation. In ascending branches of shallow circulations, the
 561 ascent is carried by mass fluxes through larger cloud-base cloud fractions, whose com-
 562 pensating subsidence is exported from the ascending regions by gravity waves. Regions
 563 with less convection import this compensating subsidence, forming descending branches
 564 of circulations (fig. 5; a visual conceptualisation is offered in fig. 1). Mesoscale circula-

565 tions in the trades are thus entirely composed of variability in condensation, rainfall, tur-
 566 bulence and waves, and are not directly driven by radiative cooling. Only at scales larger
 567 than roughly 700 km do the w_m amplitudes approach the measured and simulated campaign-
 568 average w_l associated with the wintertime climatology, and is the classical large-scale sub-
 569 sidence recovered.

570 Asking what controls w_m in the trades, is then equivalent to asking what controls
 571 the mesoscale patterning of shallow convective heating. The LES suggests that these pat-
 572 terns are not associated with variability in the surface buoyancy flux, but with cloud-
 573 layer moisture fluctuations (fig. 7), which are present in regions of mesoscale ascent up
 574 to 9 hours before the convection peaks, and which amplify due to vertical transport with
 575 the ascent (fig. 8). In this view, the mesoscale vertical motion embodies the “reverbera-
 576 tions” envisioned by Bony and Stevens (2019), between the moisture field, which sets
 577 the convection, and the convection, which sets the circulations that organise the mois-
 578 ture. Yet to fully unravel the role played by water vapour in this cloud-circulation cou-
 579 pling, we require more conclusive observations of the low-level humidity’s covariability
 580 with near-surface divergence, and better theories for mesoscale water vapour-shallow con-
 581 viction interactions. More broadly, we lack a systematic synthesis of the many mech-
 582 anisms that have in recent years been suggested to impact the mesoscale convective pat-
 583 terns in the trades. We hope such an assessment can emerge from analysis of Lagrangian
 584 trajectories - in long, large-domain LESs, in projects such as the forthcoming Lagrangian
 585 LES-MIP of EUREC⁴A, and in satellite observations. Since all suggested mechanisms
 586 appear to pass through mesoscale circulations, WTG gives a useful frame for assembling
 587 the puzzle pieces from such studies.

588 Finally, our results emphasise that km-scale trade cumuli are not passive with re-
 589 spect to their larger-scale circulations. Averaged over mesoscale domains, shallow ver-
 590 tical motion is not an unambiguous cloud-controlling factor, nor a forcing that can sim-
 591 ply be prescribed on idealised LES domains. Indeed, if the shallow clouds in the trades
 592 do respond to w_l , then the assumption is that the entire mesoscales, with all its circu-
 593 lations and associated cloud patterns, are controlled by such motion. Given the ability
 594 of the convection to self-invigorate and grow its scales, it is not obvious *a priori* how rea-
 595 sonable this assumption is. Conversely, the results underline that both mesoscale LESs
 596 and parameterisations of shallow convection must allow some exchange of the vertical
 597 motion generated by their simulated mass fluxes with adjacent mesoscale columns, if they
 598 wish to model the circulations they both currently miss (e.g. Vogel et al., 2022; Jans-
 599 sson et al., 2023). Promisingly, the data shows that ICON, at 312 m grid spacing, real-
 600 istically represents the shallow mesoscale cloud-circulation coupling. Should the ongo-
 601 ing resolution revolution of climate modelling reach such grid spacings, we may begin
 602 to glimpse the full complexity of how shallow cumuli influence our climate.

603 Open Research Section

604 The EUREC⁴A data used herein – from the ICON simulation (Schulz & Stevens,
 605 2023), JOANNE (George, Stevens, Bony, Pincus, et al., 2021) and the sounding network
 606 (Stephan et al., 2020) – is openly available through the EUREC⁴A intake catalog (EUREC4A
 607 community, 2023), see <https://howto.eurec4a.eu/intro.html>. The IASI Climate Data
 608 Record release we use is available from the EUMETSAT data store (EUMETSAT, 2022).
 609 C-2015 ASCAT data (Ricciardulli & Wentz, 2016) are produced by Remote Sensing Sys-
 610 tems and sponsored by the NASA Ocean Vector Winds Science Team. Data are avail-
 611 able at www.remss.com. The scripts used to post-process all data, and the data required
 612 to produce the figures in this paper, are available at [https://doi.org/10.5281/zenodo](https://doi.org/10.5281/zenodo.8095037)
 613 .8095037 (Janssens, 2024).

614 **Acknowledgments**

615 MJ thanks Anna Lea Albright, Franziska Glassmeier, Jordi Vilà and Raphaëla Vogel for
 616 insightful comments on an earlier version of this manuscript, and Thibaut Dauhut and
 617 Pier Siebesma for discussions. Xuanyu Chen is acknowledged for suggesting to study the
 618 simulated surface forcing along Lagrangian trajectories. MJ, GG and HS acknowledge
 619 support from the International Space Science Institute (ISSI) in Bern, through ISSI In-
 620 ternational Team project #576 (“Constraining Trade-Cumuli Feedback by Means of Pro-
 621 cess Understanding”). HS was funded by the Cooperative Institute for Climate, Ocean,
 622 & Ecosystem Studies (CICOES) under NOAA Cooperative Agreement NA20OAR4320271,
 623 Contribution No. 2024-1355. FC and DB were partly supported by CNES through the
 624 TOSCA PROCONUM project.

625 **References**

- 626 Acquistapace, C., Meroni, A. N., Labbri, G., Lange, D., Späth, F., Abbas, S., &
 627 Bellenger, H. (2022). Fast atmospheric response to a cold oceanic mesoscale
 628 patch in the north-western tropical Atlantic. *Journal of Geophysical Research: Atmo-*
 629 *spheres*, 127(21), e2022JD036799.
- 630 Adames, Á. F. (2022). The basic equations under weak temperature gradient bal-
 631 ance: Formulation, scaling, and types of convectively coupled motions. *Journal of the Atmo-*
 632 *spheric Sciences*, 79(8), 2087–2108.
- 633 Aemisegger, F., Vogel, R., Graf, P., Dahinden, F., Villiger, L., Jansen, F., ...
 634 Wernli, H. (2021). How Rossby wave breaking modulates the water cycle
 635 in the North Atlantic trade wind region. *Weather and Climate Dynamics*,
 636 2(1), 281–309.
- 637 Ahmed, F., Neelin, J. D., & Adames, Á. F. (2021). Quasi-equilibrium and weak tem-
 638 perature gradient balances in an equatorial beta-plane model. *Journal of the Atmo-*
 639 *spheric Sciences*, 78(1), 209–227.
- 640 Albrecht, B. A., Betts, A. K., Schubert, W. H., & Cox, S. K. (1979). Model of the
 641 thermodynamic structure of the trade-wind boundary layer: Part I. Theoreti-
 642 cal formulation and sensitivity tests. *Journal of Atmospheric Sciences*, 36(1),
 643 73–89.
- 644 Albright, A. L., Fildier, B., Touzé-Peiffer, L., Pincus, R., Vial, J., & Muller, C.
 645 (2021). Atmospheric radiative profiles during EUREC⁴A. *Earth System
 646 Science Data*, 13(2), 617–630.
- 647 Albright, A. L., Bony, S., Stevens, B., & Vogel, R. (2022). Observed subcloud-layer
 648 moisture and heat budgets in the trades. *Journal of the Atmospheric Sciences*,
 649 79(9), 2363–2385.
- 650 Albright, A. L., Stevens, B., Bony, S., & Vogel, R. (2023). A new conceptual picture
 651 of the trade-wind transition layer. *Journal of the Atmospheric Sciences*, 80(6),
 652 1547 – 1563.
- 653 Augstein, E., Schmidt, H., & Ostapoff, F. (1974). The vertical structure of the
 654 atmospheric planetary boundary layer in undisturbed trade winds over the
 655 Atlantic Ocean. *Boundary-layer Meteorology*, 6, 129–150.
- 656 Bellon, G., & Stevens, B. (2013). Time scales of the trade wind boundary layer ad-
 657 justment. *Journal of the atmospheric sciences*, 70(4), 1071–1083.
- 658 Betts, A. K. (1973). Non-precipitating cumulus convection and its parameterization.
 659 *Quarterly Journal of the Royal Meteorological Society*, 99(419), 178–196.
- 660 Betts, A. K., & Ridgway, W. (1989). Climatic equilibrium of the atmospheric con-
 661 vective boundary layer over a tropical ocean. *Journal of the Atmospheric Sci-
 662 ences*, 46(17), 2621–2641.
- 663 Blossey, P. N., Bretherton, C. S., Zhang, M., Cheng, A., Endo, S., Heus, T., ... Xu,
 664 K.-M. (2013). Marine low cloud sensitivity to an idealized climate change: The
 665 CGILS LES intercomparison. *Journal of Advances in Modeling Earth Systems*,
 666 5(2), 234–258.

- Bony, S., Stevens, B., Ament, F., Bigorre, S., Chazette, P., Crewell, S., ... others (2017). EUREC4A: A field campaign to elucidate the couplings between clouds, convection and circulation. *Surveys in Geophysics*, 38(6), 1529–1568.
- Bony, S., & Stevens, B. (2019). Measuring area-averaged vertical motions with dropsondes. *Journal of the Atmospheric Sciences*, 76(3), 767–783.
- Bretherton, C. S., & Park, S. (2008). A new bulk shallow-cumulus model and implications for penetrative entrainment feedback on updraft buoyancy. *Journal of the atmospheric sciences*, 65(7), 2174–2193.
- Bretherton, C. S., & Smolarkiewicz, P. K. (1989). Gravity waves, compensating subsidence and detrainment around cumulus clouds. *Journal of Atmospheric Sciences*, 46(6), 740–759.
- Bretherton, C. S., & Wyant, M. C. (1997). Moisture transport, lower-tropospheric stability, and decoupling of cloud-topped boundary layers. *Journal of the Atmospheric Sciences*, 54(1), 148–167.
- Bretherton, C. S., & Blossey, P. N. (2017). Understanding mesoscale aggregation of shallow cumulus convection using large-eddy simulation. *Journal of Advances in Modeling Earth Systems*, 9(8), 2798–2821.
- Chazette, P., Marnas, F., Totems, J., & Shang, X. (2014). Comparison of IASI water vapor retrieval with H₂O-Raman lidar in the framework of the Mediterranean HyMeX and ChArMEx programs. *Atmospheric Chemistry and Physics*, 14(18), 9583–9596.
- Chen, X., Dias, J., Wolding, B., Pincus, R., DeMott, C., Wick, G., ... Fairall, C. W. (2023). Ubiquitous sea surface temperature anomalies increase spatial heterogeneity of trade wind cloudiness on daily time scale. *Journal of the Atmospheric Sciences*, 80(12), 2969–2987.
- Chikira, M. (2014). Eastward-propagating intraseasonal oscillation represented by Chikira-Sugiyama cumulus parameterization. Part II: Understanding moisture variation under weak temperature gradient balance. *Journal of the Atmospheric Sciences*, 71(2), 615–639.
- Daleu, C. L., Plant, R. S., Woolnough, S. J., Sessions, S., Herman, M. J., Sobel, A., ... others (2015). Intercomparison of methods of coupling between convection and large-scale circulation: 1. comparison over uniform surface conditions. *Journal of Advances in Modeling Earth Systems*, 7(4), 1576–1601.
- Dauhut, T., Couvreux, F., Bouinol, D., Beucher, F., Volkmer, L., Pörtge, V., ... others (2023). Flower trade-wind clouds are shallow mesoscale convective systems. *Quarterly Journal of the Royal Meteorological Society*, 149(750), 325–347.
- Denby, L. (2020). Discovering the importance of mesoscale cloud organization through unsupervised classification. *Geophysical Research Letters*, 47(1), e2019GL085190.
- Dipankar, A., Stevens, B., Heinze, R., Moseley, C., Zängl, G., Giorgetta, M., & Brdar, S. (2015). Large eddy simulation using the general circulation model ICON. *Journal of Advances in Modeling Earth Systems*, 7(3), 963–986.
- Eastman, R., Terai, C. R., Grosvenor, D. P., & Wood, R. (2021). Evaluating the lagrangian evolution of subtropical low clouds in gcms using observations: Mean evolution, time scales, and responses to predictors. *Journal of the Atmospheric Sciences*, 78(2), 353–372.
- Emanuel, K. (2019). Inferences from simple models of slow, convectively coupled processes. *Journal of the Atmospheric Sciences*, 76(1), 195–208.
- Emanuel, K. A., David Neelin, J., & Bretherton, C. S. (1994). On large-scale circulations in convecting atmospheres. *Quarterly Journal of the Royal Meteorological Society*, 120(519), 1111–1143.
- EUMETSAT. (2021). *Validation report IASI level-2 T and q profiles* (Tech. Rep. No. Release 1). European Organisation for the Exploitation of Meteorological Satellites. doi: 10.15770/EUM\SEC\CLM\0027

- EUMETSAT. (2022). *IASI all sky temperature and humidity profiles* (Tech. Rep. No. Climate Data Record Release 1.1 - Metop-A and -B). European Organisation for the Exploitation of Meteorological Satellites. Retrieved from <http://doi.org/10.15770/EUM\SEC\CLM\0063> doi: 10.15770/EUM\SEC\CLM\0063
- EUREC4A community. (2023, October). *Eurec4a*. Zenodo. Retrieved from <https://doi.org/10.5281/zenodo.8422322> doi: 10.5281/zenodo.8422322
- Fildier, B., Muller, C., Pincus, R., & Fueglistaler, S. (2023). How moisture shapes low-level radiative cooling in subsidence regimes. *AGU Advances*. doi: <https://doi.org/10.1029/2023AV000880>
- George, G., Stevens, B., Bony, S., Klingebiel, M., & Vogel, R. (2021). Observed impact of mesoscale vertical motion on cloudiness. *Journal of the Atmospheric Sciences*, 78(8), 2413–2427.
- George, G., Stevens, B., Bony, S., Pincus, R., Fairall, C., Schulz, H., ... others (2021). JOANNE: Joint dropsonde observations of the atmosphere in tropical north atlantic meso-scale environments. *Earth System Science Data*, 13(11), 5253–5272.
- George, G., Stevens, B., Bony, S., Vogel, R., & Naumann, A. K. (2023). Widespread shallow mesoscale circulations observed in the trades. *Nature Geoscience*. doi: 10.1038/s41561-023-01215-1
- Golaz, J.-C., Larson, V. E., & Cotton, W. R. (2002). A PDF-based model for boundary layer clouds. Part I: Method and model description. *Journal of the Atmospheric Sciences*, 59(24), 3540–3551.
- Held, I. M., & Hoskins, B. J. (1985). Large-scale eddies and the general circulation of the troposphere. *Advances in geophysics*, 28 Part A, 3–31.
- Hourdin, F., Jam, A., Rio, C., Couvreux, F., Sandu, I., Lefebvre, M.-P., ... Idelkadi, A. (2019). Unified parameterization of convective boundary layer transport and clouds with the thermal plume model. *Journal of Advances in Modeling Earth Systems*, 11(9), 2910–2933.
- Janssens, M. (2024, April). *Supporting data for "Shallow convective heating in weak temperature gradient balance explains mesoscale vertical motions in the trades" (previously for ch. 5 of "Mesoscale Cloud Patterns in the Trade-Wind Boundary Layer")*. Zenodo. Retrieved from <https://doi.org/10.5281/zenodo.10998663> doi: 10.5281/zenodo.10998663
- Janssens, M., De Arellano, J. V.-G., Van Heerwaarden, C. C., De Roode, S. R., Siebesma, A. P., & Glassmeier, F. (2023). Nonprecipitating shallow cumulus convection is intrinsically unstable to length scale growth. *Journal of the Atmospheric Sciences*, 80(3), 849–870.
- Janssens, M., Vilà-Guerau De Arellano, J., Scheffer, M., Antonissen, C., Siebesma, A. P., & Glassmeier, F. (2021). Cloud patterns in the trades have four interpretable dimensions. *Geophysical Research Letters*, 48(5), e2020GL091001.
- Jansson, F., Janssens, M., Grönqvist, J. H., Siebesma, P., Glassmeier, F., Attema, J. J., ... others (2023). Cloud botany: Shallow cumulus clouds in an ensemble of idealized large-domain large-eddy simulations of the trades. *Journal of Advances in Modeling Earth Systems*, 10, e2023MS003796.
- Klein, R. (2010). Scale-dependent models for atmospheric flows. *Annual Review of Fluid Mechanics*, 42, 249–274.
- Klein, S. A., Hall, A., Norris, J. R., & Pincus, R. (2017). Low-cloud feedbacks from cloud-controlling factors: a review. In R. Pincus, M. Winker, S. Bony, & B. Stevens (Eds.), *Shallow clouds, water vapor, circulation, and climate sensitivity* (pp. 135–157). Springer.
- Klingebiel, M., Konow, H., & Stevens, B. (2021). Measuring shallow convective mass flux profiles in the trade wind region. *Journal of the Atmospheric Sciences*, 78(10), 3205–3214.
- Klinger, C., Mayer, B., Jakub, F., Zinner, T., Park, S.-B., & Gentine, P. (2017). Ef-

- 777 fects of 3-D thermal radiation on the development of a shallow cumulus cloud
 778 field. *Atmospheric Chemistry and Physics*, 17(8), 5477–5500.
- 779 Konow, H., Ewald, F., George, G., Jacob, M., Klingebiel, M., Kölling, T., ... others
 780 (2021). EUREC4A's HALO. *Earth System Science Data*, 13(12), 5545–5563.
- 781 Kuang, Z. (2008). Modeling the interaction between cumulus convection and linear
 782 gravity waves using a limited-domain cloud system-resolving model. *Journal of*
 783 *the Atmospheric Sciences*, 65(2), 576–591.
- 784 Lamer, K., Kollrias, P., & Nuijens, L. (2015). Observations of the variability of shal-
 785 low trade wind cumulus cloudiness and mass flux. *Journal of Geophysical Re-*
 786 *search: Atmospheres*, 120(12), 6161–6178.
- 787 Lewis, H., Bellon, G., & Dinh, T. (2023). Upstream large-scale control of subtropical
 788 low-cloud climatology. *Journal of Climate*, 36(10), 3289–3303.
- 789 Mapes, B. E. (1993). Gregarious tropical convection. *Journal of Atmospheric Sci-*
 790 *ences*, 50(13), 2026–2037.
- 791 Menzel, W. P., Schmit, T. J., Zhang, P., & Li, J. (2018). Satellite-based atmospheric
 792 infrared sounder development and applications. *Bulletin of the American Mete-*
 793 *orological Society*, 99(3), 583–603.
- 794 Muller, C. J., Yang, D., Craig, G., Cronin, T., Fildier, B., Haerter, J. O., ... others
 795 (2022). Spontaneous aggregation of convective storms. *Annual Review of Fluid*
 796 *Mechanics*, 54, 133–157.
- 797 Myers, T. A., & Norris, J. R. (2013). Observational evidence that enhanced sub-
 798 sidence reduces subtropical marine boundary layer cloudiness. *Journal of Cli-*
 799 *mate*, 26(19), 7507–7524.
- 800 Narenpitak, P., Kazil, J., Yamaguchi, T., Quinn, P. K., & Feingold, G. (2021).
 801 From sugar to flowers: A transition of shallow cumulus organization dur-
 802 ing ATOMIC. *Journal of Advances in Modeling Earth Systems*, 13,
 803 e2021MS002619.
- 804 Narenpitak, P., Kazil, J., Yamaguchi, T., Quinn, P. K., & Feingold, G. (2023). The
 805 Sugar-to-Flower shallow cumulus transition under the influences of diel cycle
 806 and free-tropospheric mineral dust. *Journal of Advances in Modeling Earth*
 807 *Systems*, 15(1), e2022MS003228.
- 808 Naumann, A. K., Stevens, B., Hohenegger, C., & Mellado, J. P. (2017). A concep-
 809 tual model of a shallow circulation induced by prescribed low-level radiative
 810 cooling. *Journal of the Atmospheric Sciences*, 74(10), 3129–3144.
- 811 Naumann, A. K., Stevens, B., & Hohenegger, C. (2019). A moist conceptual model
 812 for the boundary layer structure and radiatively driven shallow circulations in
 813 the trades. *Journal of the Atmospheric Sciences*, 76(5), 1289–1306.
- 814 Neggers, R. A. J., Stevens, B., & Neelin, J. D. (2006). A simple equilibrium model
 815 for shallow-cumulus-topped mixed layers. *Theoretical and Computational Fluid*
 816 *Dynamics*, 20, 305–322.
- 817 Nicholls, M. E., Pielke, R. A., & Cotton, W. R. (1991). Thermally forced gravity
 818 waves in an atmosphere at rest. *Journal of the atmospheric sciences*, 48(16),
 819 1869–1884.
- 820 Nuijens, L., Stevens, B., & Siebesma, A. P. (2009). The environment of precipitat-
 821 ing shallow cumulus convection. *Journal of the Atmospheric Sciences*, 66(7),
 822 1962–1979.
- 823 Nuijens, L., Serikov, I., Hirsch, L., Lonitz, K., & Stevens, B. (2014). The distribu-
 824 tion and variability of low-level cloud in the North Atlantic trades. *Quarterly*
 825 *Journal of the Royal Meteorological Society*, 140(684), 2364–2374.
- 826 Park, K.-A., Cornillon, P., & Codiga, D. L. (2006). Modification of surface winds
 827 near ocean fronts: Effects of Gulf Stream rings on scatterometer (QuikSCAT,
 828 NSCAT) wind observations. *Journal of Geophysical Research: Oceans*,
 829 111(C3).
- 830 Prange, M., Buehler, S. A., & Brath, M. (2023). How adequately are elevated moist
 831 layers represented in reanalysis and satellite observations? *Atmospheric Chem-*

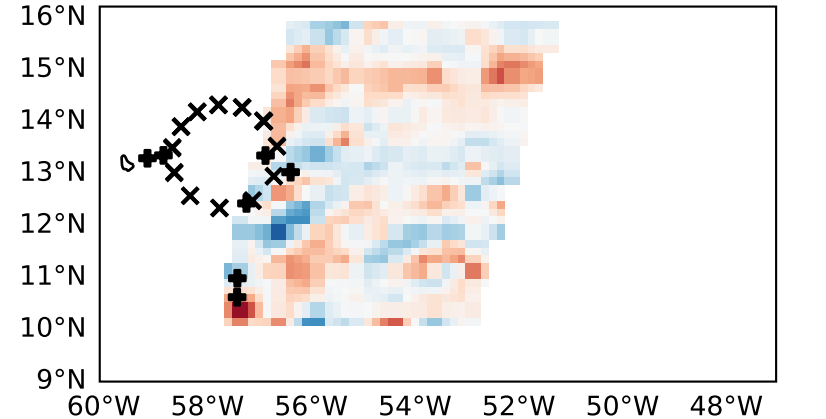
- 832 *istry and Physics*, 23(1), 725–741.
- 833 Radtke, J., Vogel, R., Ament, F., & Naumann, A. K. (2023). Spatial organisation
834 affects the pathway to precipitation in simulated trade-wind convection. *Au-*
835 *thorea*. doi: <https://doi.org/10.22541/essoar.167979635.58663858/v1>
- 836 Raymond, D. J., & Zeng, X. (2005). Modelling tropical atmospheric convection in
837 the context of the weak temperature gradient approximation. *Quarterly Jour-*
838 *nal of the Royal Meteorological Society: A journal of the atmospheric sciences,*
839 *applied meteorology and physical oceanography*, 131(608), 1301–1320.
- 840 Raymond, D. J. (1995). Regulation of moist convection over the west Pacific warm
841 pool. *Journal of Atmospheric Sciences*, 52(22), 3945–3959.
- 842 Raymond, D. J., Sessions, S. L., Sobel, A. H., & Fuchs, Ž. (2009). The mechanics of
843 gross moist stability. *Journal of Advances in Modeling Earth Systems*, 1(3), #
844 9.
- 845 Raymond, D. J., Fuchs, Ž., Gjorgjevska, S., & Sessions, S. (2015). Balanced dynam-
846 ics and convection in the tropical troposphere. *Journal of Advances in Model-*
847 *ing Earth Systems*, 7(3), 1093–1116.
- 848 Ricciardulli, L., & Wentz, F. (2016). *ASCAT C-2015 daily ocean vector winds on*
849 *0.25 deg grid* (Tech. Rep. No. Version 02.1 Daily). Remote Sensing Systems.
850 Retrieved from www.remss.com
- 851 Romps, D. M. (2012a). Numerical tests of the weak pressure gradient approxima-
852 *tion*. *Journal of the atmospheric sciences*, 69(9), 2846–2856.
- 853 Romps, D. M. (2012b). Weak pressure gradient approximation and its analytical
854 solutions. *Journal of the Atmospheric Sciences*, 69(9), 2835 - 2845. Re-
855 trieved from <https://journals.ametsoc.org/view/journals/atsc/69/9/jas-d-11-0336.1.xml> doi: 10.1175/JAS-D-11-0336.1
- 856 Saffin, L., Lock, A., Tomassini, L., Blyth, A., Böing, S., Denby, L., & Marsham, J.
857 (2023). Kilometer-scale simulations of trade-wind cumulus capture processes
858 of mesoscale organization. *Journal of Advances in Modeling Earth Systems*,
859 15(3), e2022MS003295.
- 860 Sakradzija, M., & Klingebiel, M. (2020). Comparing ground-based observations
861 and a large-eddy simulation of shallow cumuli by isolating the main controlling
862 factors of the mass flux distribution. *Quarterly Journal of the Royal Meteoro-*
863 *logical Society*, 146(726), 254–266.
- 864 Savazzi, A. C., Nuijens, L., De Rooy, W., Janssens, M., & Siebesma, A. P. (2024).
865 Momentum transport in organized shallow cumulus convection. *Journal of the*
866 *Atmospheric Sciences*, 81(2), 279–296.
- 867 Schulz, H., & Stevens, B. (2023). Evaluating large-domain, hecto-meter, large-eddy
868 simulations of trade-wind clouds using eurec4a data. *Journal of Advances in*
869 *Modeling Earth Systems*, 15(10), e2023MS003648.
- 870 Schulz, H., & Stevens, B. (2018). Observing the tropical atmosphere in moisture
871 space. *Journal of the Atmospheric Sciences*, 75(10), 3313–3330.
- 872 Schulz, H. (2022). C3ontext: a common consensus on convective organization during
873 the EUREC4A experiment. *Earth System Science Data*, 14(3), 1233–1256.
- 874 Scott, R. C., Myers, T. A., Norris, J. R., Zelinka, M. D., Klein, S. A., Sun, M., &
875 Doelling, D. R. (2020). Observed sensitivity of low-cloud radiative effects
876 to meteorological perturbations over the global oceans. *Journal of Climate*,
877 33(18), 7717–7734.
- 878 Siebesma, A. P., Bretherton, C. S., Brown, A., Chlond, A., Cuxart, J., Duynkerke,
879 P. G., ... others (2003). A large eddy simulation intercomparison study of
880 shallow cumulus convection. *Journal of the Atmospheric Sciences*, 60(10),
881 1201–1219.
- 882 Sobel, A. H., & Bretherton, C. S. (2000). Modeling tropical precipitation in a single
883 column. *Journal of Climate*, 13(24), 4378–4392.
- 884 Sobel, A. H., Nilsson, J., & Polvani, L. M. (2001). The weak temperature gradi-
885 ent approximation and balanced tropical moisture waves. *Journal of the Atmo-*
886

- 887 *spheric Sciences*, 58(23), 3650–3665.
- 888 Stephan, C. C., & Mariaccia, A. (2021). The signature of the tropospheric gravity
889 wave background in observed mesoscale motion. *Weather and Climate Dynamics*,
890 2(2), 359–372.
- 891 Stephan, C. C., Schnitt, S., Schulz, H., Bellenger, H., De Szoek, S. P., Ac-
892 quistapace, C., ... others (2020). Ship-and island-based atmospheric soundings
893 from the 2020 eurec 4 a field campaign. *Earth System Science Data Discus-*
894 *sions*, 2020, 1–35.
- 895 Stevens, B., Ackerman, A. S., Albrecht, B. A., Brown, A. R., Chlond, A., Cuxart, J.,
896 ... others (2001). Simulations of trade wind cumuli under a strong inversion.
897 *Journal of the Atmospheric Sciences*, 58(14), 1870–1891.
- 898 Stevens, B. (2006). Bulk boundary-layer concepts for simplified models of tropical
899 dynamics. *Theoretical and Computational Fluid Dynamics*, 20(5), 279–304.
- 900 Stevens, B. (2007). On the growth of layers of nonprecipitating cumulus convection.
901 *Journal of the Atmospheric Sciences*, 64(8), 2916–2931.
- 902 Stevens, B., & Seifert, A. (2008). Understanding macrophysical outcomes of micro-
903 physical choices in simulations of shallow cumulus convection. *Journal of the*
904 *Meteorological Society of Japan. Ser. II*, 86, 143–162.
- 905 Stevens, B., Brogniez, H., Kiemle, C., Lacour, J.-L., Crevoisier, C., & Kiliani, J.
906 (2018). Structure and dynamical influence of water vapor in the lower tropical
907 troposphere. In R. Pincus, M. Winker, S. Bony, & B. Stevens (Eds.), *Shal-*
908 *low clouds, water vapor, circulation, and climate sensitivity* (pp. 199–225).
909 Springer.
- 910 Stevens, B., Bony, S., Brogniez, H., Hentgen, L., Hohenegger, C., Kiemle, C., ...
911 others (2020). Sugar, gravel, fish and flowers: Mesoscale cloud patterns in the
912 trade winds. *Quarterly Journal of the Royal Meteorological Society*, 146(726),
913 141–152.
- 914 Stevens, B., Bony, S., Farrell, D., Ament, F., Blyth, A., Fairall, C., ... others
915 (2021). EUREC4A. *Earth System Science Data*, 13(8), 4067–4119.
- 916 Van Zanten, M. C., Stevens, B., Nuijens, L., Siebesma, A. P., Ackerman, A., Burnet,
917 F., ... others (2011). Controls on precipitation and cloudiness in simulations
918 of trade-wind cumulus as observed during RICO. *Journal of Advances in*
919 *Modeling Earth Systems*, 3(2).
- 920 Vilà-Guerau De Arellano, J., Van Heerwaarden, C., Van Stratum, B., & Van
921 Den Dries, K. (2015). *Atmospheric boundary layer: Integrating air chem-*
922 *istry and land interactions*. Cambridge University Press Cambridge.
- 923 Villiger, L., Wernli, H., Boettcher, M., Hagen, M., & Aemisegger, F. (2022). La-
924 grangian formation pathways of moist anomalies in the trade-wind region dur-
925 ing the dry season: Two case studies from EUREC4A. *Weather and Climate*
926 *Dynamics*, 3(1), 59–88.
- 927 Vogel, R., Albright, A. L., Vial, J., George, G., Stevens, B., & Bony, S. (2022).
928 Strong cloud–circulation coupling explains weak trade cumulus feedback. *Na-*
929 *ture*, 612, 696–700.
- 930 Walters, D., Baran, A. J., Boutle, I., Brooks, M., Earnshaw, P., Edwards, J., ...
931 others (2019). The met office unified model global atmosphere 7.0/7.1 and
932 jules global land 7.0 configurations. *Geoscientific Model Development*, 12(5),
933 1909–1963.
- 934 Wolding, B. O., Maloney, E. D., & Branson, M. (2016). Vertically resolved weak
935 temperature gradient analysis of the m adden-j ulian o scillation in sp-cesm.
936 *Journal of Advances in Modeling Earth Systems*, 8(4), 1586–1619.
- 937 Wood, R., & Field, P. R. (2011). The distribution of cloud horizontal sizes. *Journal*
938 *of Climate*, 24(18), 4800–4816.
- 939 Yang, D. (2021). A shallow-water model for convective self-aggregation. *Journal of*
940 *the Atmospheric Sciences*, 78(2), 571–582.
- 941 Yin, B., & Albrecht, B. A. (2000). Spatial variability of atmospheric boundary layer

942 structure over the eastern equatorial Pacific. *Journal of Climate*, 13(9), 1574–
943 1592.

Figure 2.

ASCAT



ICON

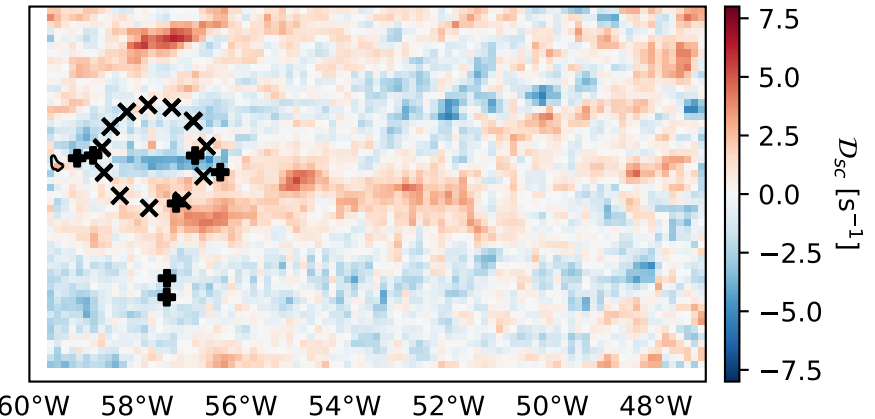


Figure 8.

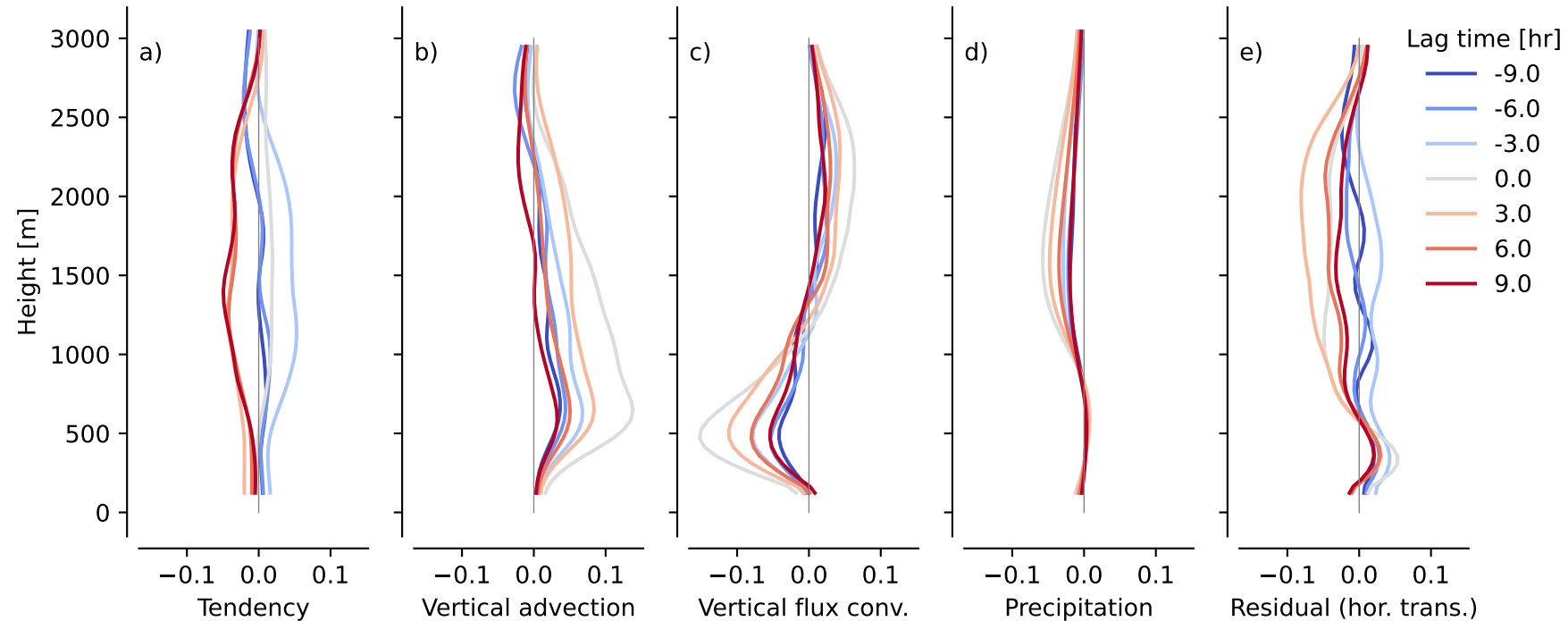


Figure 1.

"Diverging" block / descending branch

"Converging" block / ascending branch

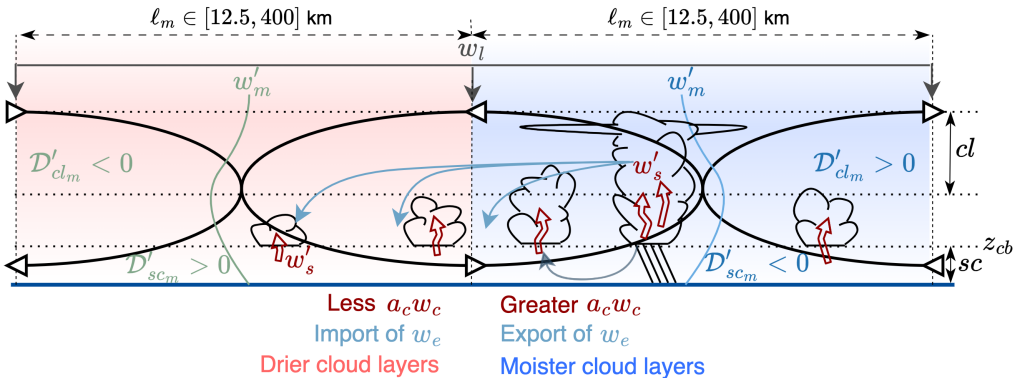


Figure 7.

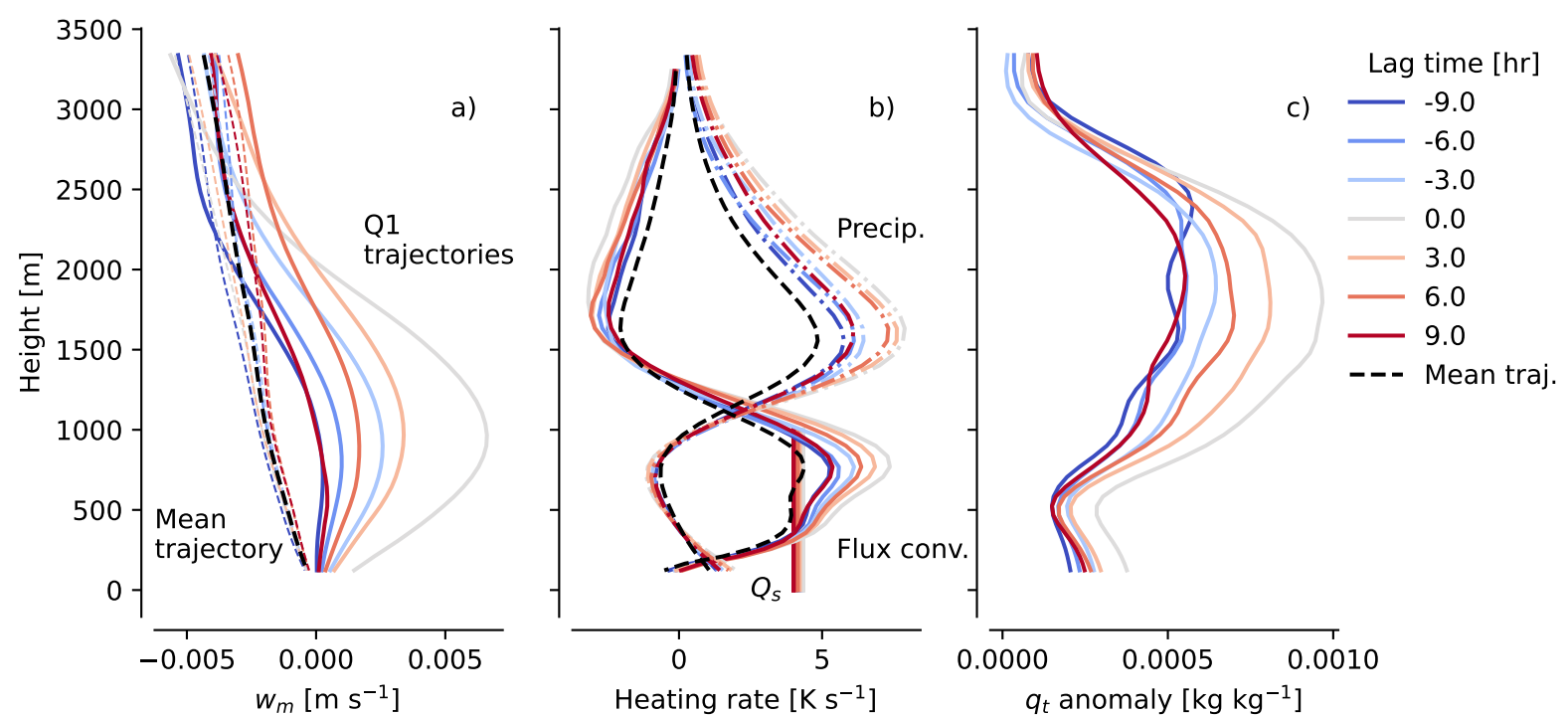


Figure 3.

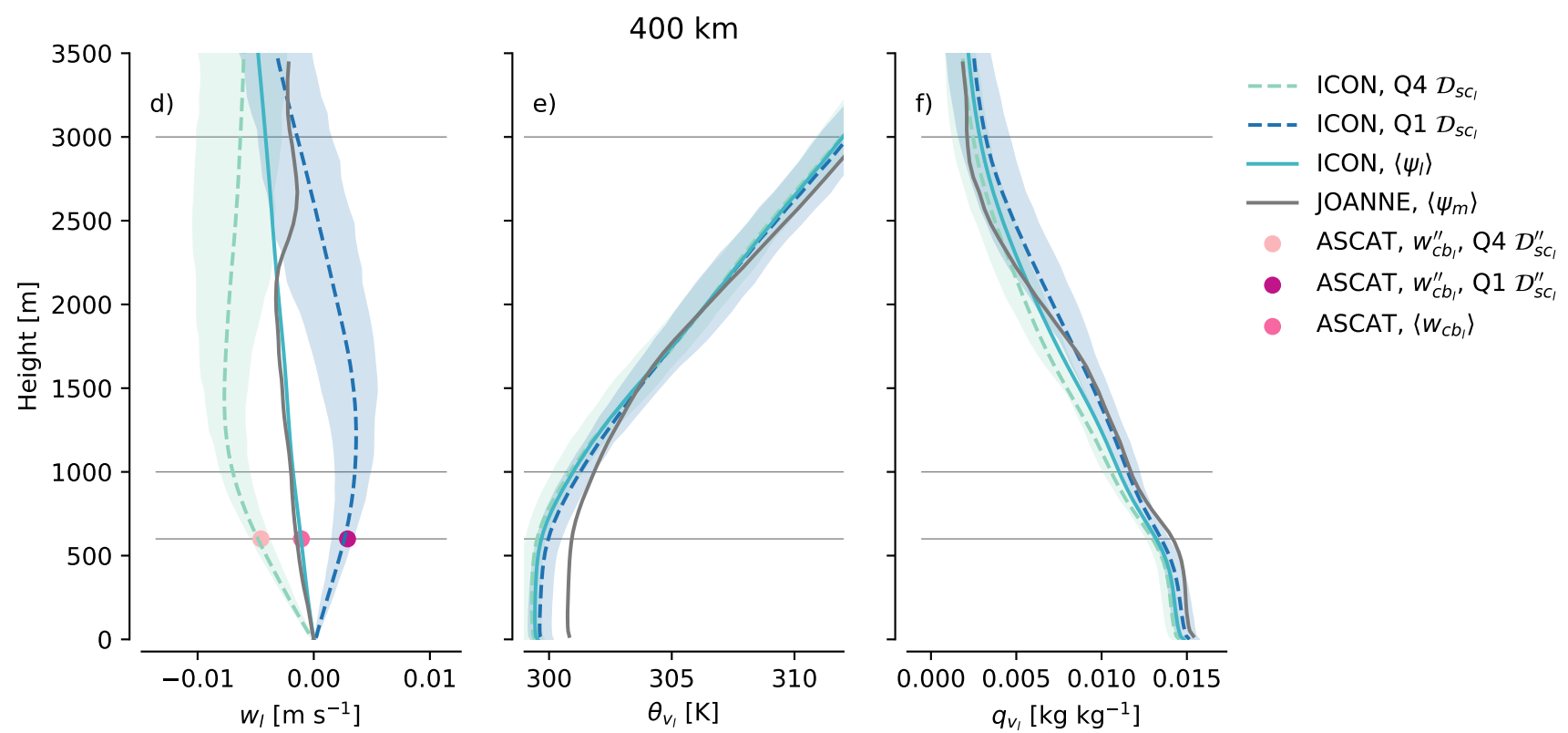
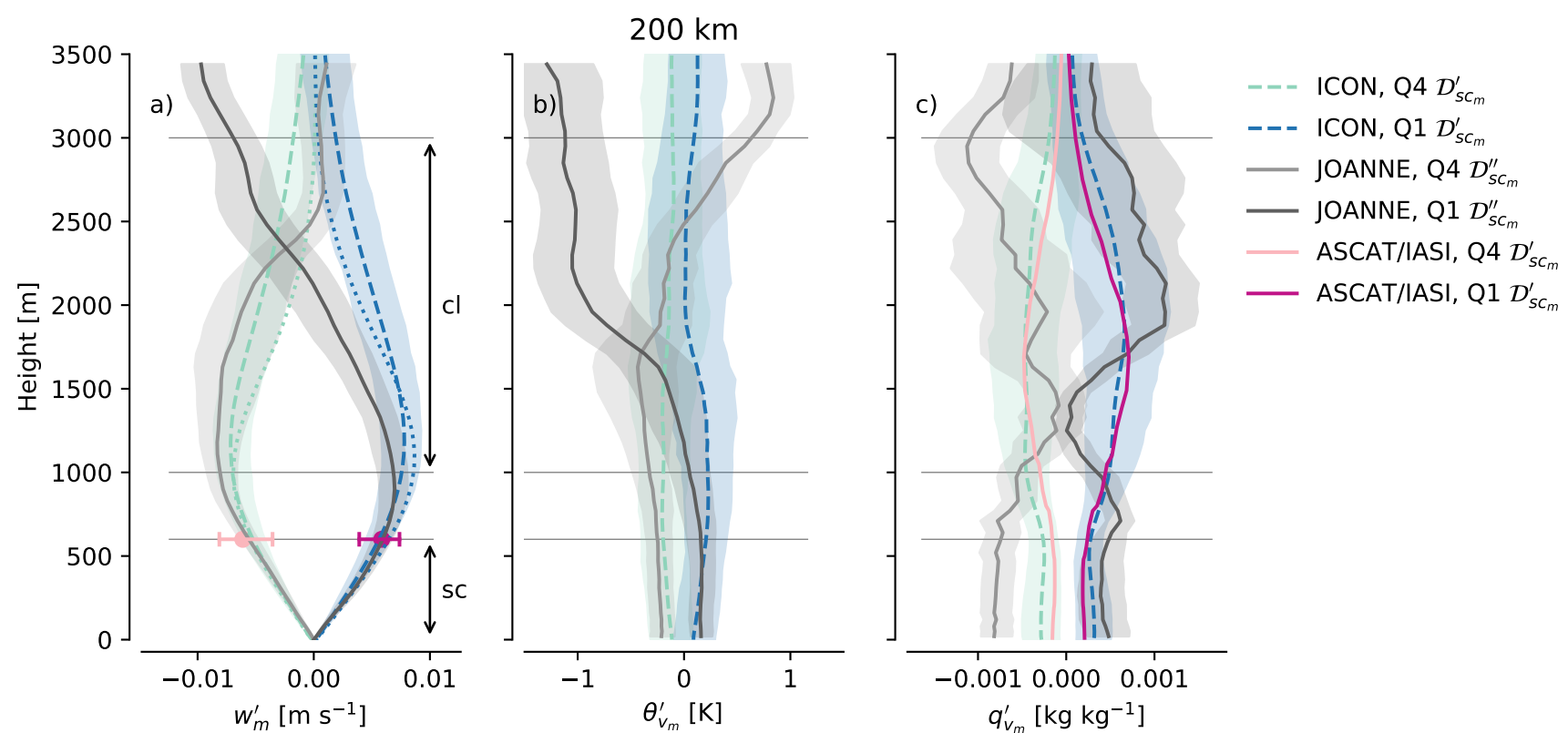


Figure 6.

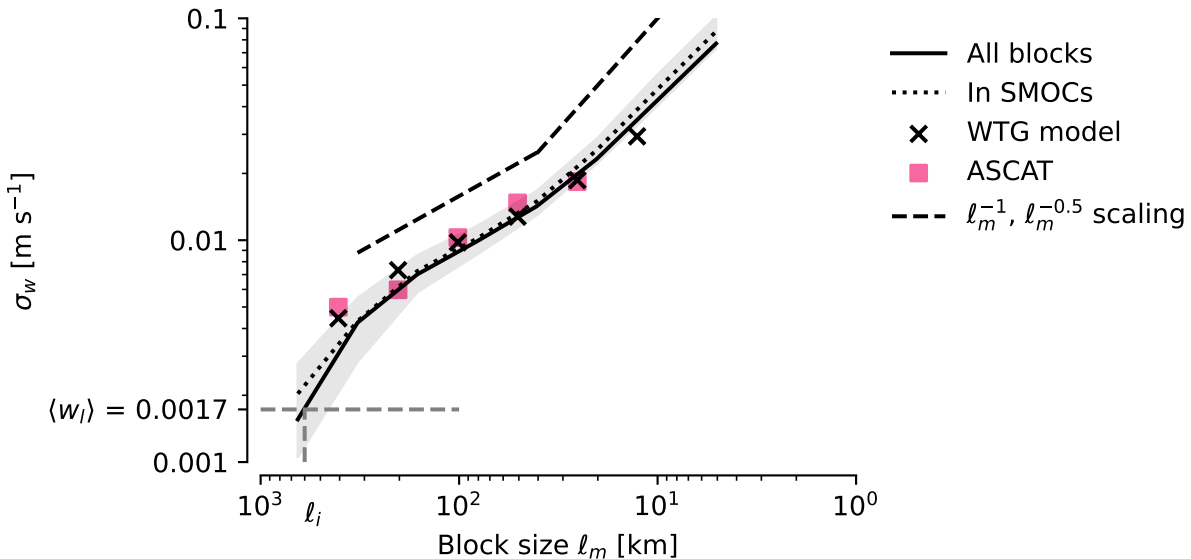


Figure 5.

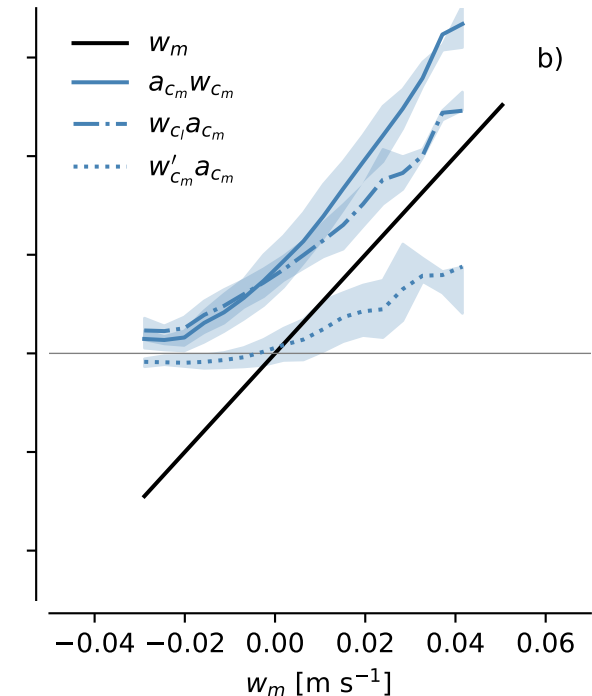
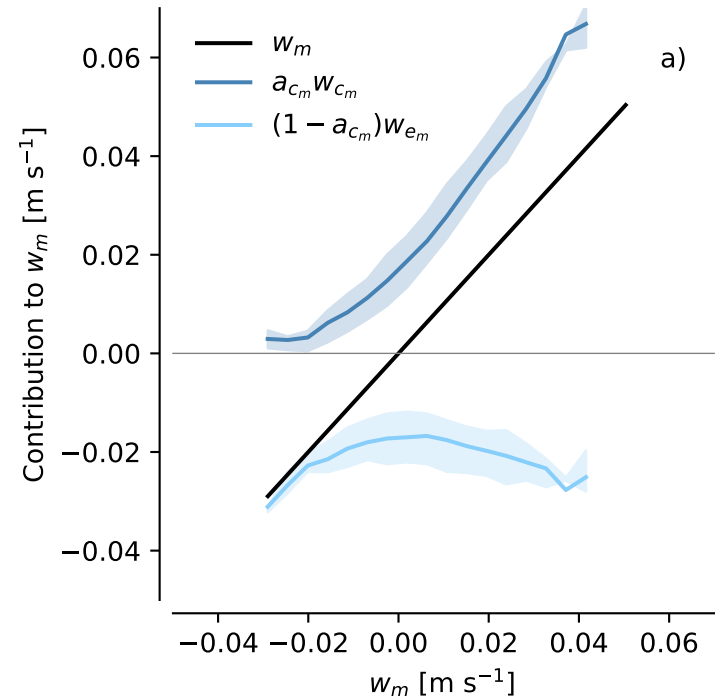


Figure 4.

